2010-11-19

Improved Measurement and Separation Techniques for Interior Near-field Acoustical Holography

Zachary A. Collins

Brigham Young University - Provo

Improved Measurement and Separation

Techniques for Interior Near-field

Acoustical Holography

Zachary A. Collins

A thesis submitted to the faculty of
Brigham Young University
in partial fulfillment of the requirements for the degree of

Master of Science

Jonathan D. Blotter, Chair
Scott D. Sommerfeldt
Kent L. Gee

Department of Mechanical Engineering

Brigham Young University

December 2010

ABSTRACT

Improved Measurement and Separation

Techniques for Interior Near-field

Acoustical Holography

Zachary A. Collins

Department of Mechanical Engineering

Master of Science

Recent advances in near-field acoustical holography (NAH) have expanded the theory to interior spaces where multiple sources and/or reflections are present. In 1990, Tamura presented the spatial Fourier transform separation method to measure the reflection coefficient at oblique angles using two measurement planes in the wave number domain. This paper adapts the spatial Fourier transform separation method for application in interior NAH. A practical exploration of important experimental parameters is performed, which include the relative amplitudes of primary and disturbing sources, the measurement plane separation distance, and an acceptable noise floor. This technique is successfully applied in a reverberant environment to reconstruct the velocity of a clamped vibrating plate.

NAH methods based on the measurement of pressure and particle velocity have led to the ability to reduce the required measurement locations. Other recent advances in NAH have expanded the theory to interior spaces where multiple sources and/or reflections are present. This paper investigates the use of interpolation techniques to reduce the required measurement locations for interior NAH. Specifically, the benefits of a bi-cubic Hermite surface patch interpolation are discussed and compared to other interpolation routines. Although the required inputs for the Hermite interpolation can be measured using a variety of devices, a scanning six-microphone probe in a tetrahedral configuration is suggested. The six microphones are utilized to simultaneously sample pressure on two parallel planes and estimate the pressure gradients on both of these planes. The two interpolated measurement holograms are used to separate the incoming and outgoing waves using the spatial Fourier-transform method. Analytical simulations of simply supported plates are shown as well as experimental results in a reverberation room to characterize the reduction in measurement locations. Depending on the spatial frequency of the hologram, a measurement location reduction of 20–80% was observed.

Keywords: Zachary Collins, Fourier, NAH, interior, acoustics, near-field acoustical holography, interpolation, particle velocity, wave separation, Tamura, six-microphone probe

ACKNOWLEDGMENTS

TABLE OF CONTENTS

LIST OF TABLES

x

LIST OF FIGURES

1 INTRODUCTION

This chapter presents motivation for my research and an introduction into noise identification, near-field acoustical holography, wave separation, and measurement field interpolation. It also presents research objectives and goals and an outline for the remaining chapters of this thesis.

1.1 Motivation

Our lives are surrounded by noise. Although our ears are sensitive devices able to detect a wide array of frequencies and even the direction noises come from, they are often unable to pinpoint the direction of noise in an interior space. Furthermore, if information about vibration induced noise is needed to control the noise, the ear is not able to tell how something is vibrating. The research presented in this thesis helps to identify and characterize noise sources even in interior spaces. Of course, there are other devices and techniques to help identify and characterize noise sources, which will be discussed in the next section, but few techniques provide more information than near-field acoustical holography.

1.2 Background

To understand the contributions of this thesis, it will be helpful to introduce the following topics.

1.2.1 Noise Identification

The field of acoustic imaging is very broad and its applications may be found in medical ultrasonic diagnosis, nondestructive evaluations and testing, sound navigation imaging, SONAR, and other underwater acoustic imaging. Noise identification is useful in the military for underwater naval purposes, as well as for automotive, aircraft, appliance and machinery manufacturers. In most cases, identifying the root causes of undesirable noise and vibration, as well as the relationship between the two, are the first steps to creating a better quality product.

There are numerous techniques that are used for noise identification. One method involves using a microphone to compute the sound pressure level (SPL) wherever the microphone is held. Another technique involves using two phase-matched microphones to compute the sound intensity coming from a source.[1] More complex forms of acoustic imaging include beamforming,[2] inverse frequency response function methods,[3] inverse finite-element,[4] and time reversal methods.[5]

Of all the techniques available to visualize noise sources, near-field acoustical holography (NAH) offers advantages because "it enables one to reconstruct all acoustic quantities such as the acoustic pressure, particle velocity, and acoustic intensity not only at a measurement location but in 3D space and on a source surface by measuring the acoustic pressure in the near field of the target source surface. Moreover, they allow for visualization of the structural waves traveling along the surface of a structure, yielding an invaluable insight into the interrelationship between sound and vibrations."[6]

1.2.2 Near-Field Acoustical Holography

First presented by Williams in 1980,[7] NAH allows information about a three-dimensional sound field to be known by making a two-dimensional 'hologram' measurement. When a

surface vibrates, it typically radiates noise. Not all the noise coming from a vibrating object reaches the far-field; there exists evanescent waves that decay exponentially as they move away from the source. NAH is typically performed by making a sound pressure measurement along a two-dimensional plane over the top of a source. This technique is used to predict what the pressure is in time and space throughout the environment. In additional to discovering information about the pressure, the particle velocity can also be reconstructed. With the addition of particle velocity, it is possible to know information about the sound power, and the sound intensity in the field. NAH is most useful when a vibrating source, such as an engine or a car door needs to be visualized. The velocity and pressure on a surface can be solved for; this leads to an unlimited supply of information available for the user.

1.3 Contributions

The benefits of this work advance the field of knowledge in the area of near-field acoustical holography by applying a detailed method of wave separation for NAH in interior fields. Important parameters were documented to help users understand how to use this method. Investigated parameters include the relative source strengths, the measurement plane separation distance, and the required signal to noise ratio. This research will also add to the current body of knowledge by introducing a measurement technique that is relatively simple and inexpensive and which reduces the number of measurements that need to be taken. To aid with this research, a portable automated linear positioning unit was built and programmed to automatically take microphone measurements in two directions. This new device will aid further research in the BYU Acoustics Research Group. Two manuscripts have been prepared for submission to the *Journal of the Acoustical Society of America*.

1.4   Overview

Chapter 2 discusses past work to show the foundation that was built upon. Chapter 3 is a manuscript being prepared for submission to the *Journal of the Acoustical Society of America* regarding the application of the spatial Fourier transform wave separation method to interior NAH. Chapter 4 is a manuscript being prepared for submission to the *Journal of the Acoustical Society of America* regarding a new measurement technique to reduce the number of measurements for interior NAH. Chapter 5 details the conclusions and suggested future work on this topic. An appendix is also included to explain how to set up and use the portable linear positioning system developed for this research. The appendix also includes a copy of the code used for numerical simulations and data manipulation.

2 PRIOR WORK

2.1 Near-Field Acoustical Holography

Holographic measurements are used to discover information about a three-dimensional field. Acoustic holography is the process of using a two-dimensional plane of pressure measurements to discover information about a three-dimensional acoustic field. To find information about an acoustic field in the near-field of a source, pressure measurements must be made close to the source to ensure evanescent waves have been included in the measurement. In 1980 Williams introduced a method to perform acoustic holography in the near-field using simple transfer functions in the wave number domain.[7] This Fourier transform-based method of near-field acoustical holography (NAH) can be used to identify and characterize noise sources and the process is outlined in Figure 2-1.
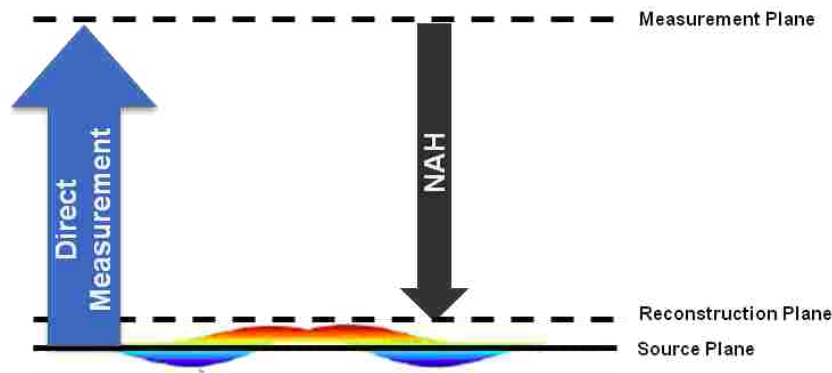
Figure 2-1: The planes involved in performing NAH in Cartesian coordinates. A measurement is made in the near-field, then NAH is used to propagate back towards the source plane.

Limitations in this conventional form of NAH have led to the development of other methods. Although the original form was computationally efficient and could perform

reconstructions for each frequency in a matter of seconds, these other forms are often more computationally expensive, but allow for additional application. To overcome the fact that arbitrary geometries cannot be analyzed, a singular value decomposition method[8] and an IBEM[9] method were developed. To overcome the requirement that the measurement plane must be conformal to the source with a separable geometry, the Helmholtz equation least-squares method was developed.[10] To neglect the requirement that the measurement plane needs to be four times bigger than the source and to allow for arbitrary geometries, patch NAH using a statistically optimized NAH (SONAH) was developed.[11]

2.2 Interior Near-Field Acoustical Holography

One of the most restrictive assumptions for the original NAH method is that all sources radiate into a free-field and that a reconstruction cannot be obtained on a surface behind any sources. Unfortunately, many practical situations where noise source identification would be advantageous take place in an enclosed space where reflections are present or in a space where multiple sources are radiating.

Recently, the application of NAH to interior fields or fields with multiple sources has been the focus of much research. Villot, et al. provided a method to perform NAH in a semi-infinite rectangular duct.[12] Kim, et al. showed that by modifying the original formulation of NAH to include boundary conditions, reflections can be built into NAH reconstructions.[13] Williams, et al. demonstrated how NAH can be performed inside an aircraft using a combination of NAH and BEM.[14] Jacobsen and Jaud presented the '*p-u method,*' where a simultaneous pressure and normal particle velocity measurement plane allows the contribution of a disturbing source directly opposite the primary source to be negated through an averaging technique.[15] Zhang, et al. showed a modification of this method where the disturbing source is not required to

6

be symmetric with the primary source.[16] Although it improved the original '*p-u method,*' this technique only provided descent results at low frequencies.

In 1990 Tamura developed a method to calculate the reflection coefficients at oblique angles by using two planes of measurements to separate the incident and reflected waves from a surface.[17] Experimental validation of this paper was published in 1995.[18] Although originally developed for application in reflection and absorption purposes, this technique lends itself to application in the field of NAH. Because the separation is performed in the wave number domain through the use of a spatial Fourier transform, it only adds a few more lines of quick code to an already efficient method. Cheng published how this technique could be used to separate the incident and scattered waves off an arbitrary object.[19] Although many papers discussing methods to perform NAH in interior spaces cite Tamura's method, no one has published how to adapt his method to NAH. Furthermore, very few limitations and advantages of this method are discussed.

Implementation of this wave separation technique requires measurements to be made on two parallel measurement planes. Once the separation has occurred, the original implementation of NAH can be performed to propagate back towards the source, as shown in Figure 2-2.
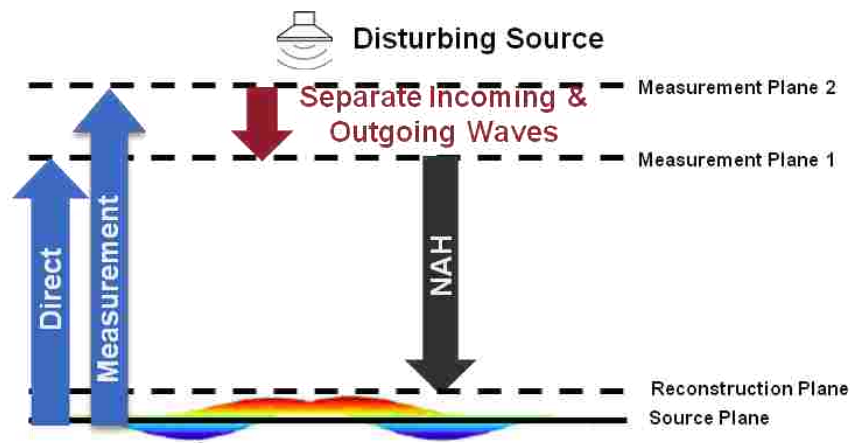
Figure 2-2: The planes involved in performing NAH in an interior space or when a disturbing source is present. The wave separation requires measurements to be made on two parallel planes before propagation.

2.3 Interpolation for NAH

NAH requires a large number of measurements to represent an acoustic field. Harris[20] was able to show that the number of sensors required to create an adequate hologram can be reduced by also measuring the particle velocity at each location. This particle velocity can be used to approximate the pressure gradient which can be used to create a bi-cubic Hermite surface interpolation patch between each measurement point. This pressure field interpolation was shown to reduce the number of measurement locations by 70%.

This paper explains how by using this same interpolation method, the number of required measurement locations can be reduced through the use of a probe with multiple microphones. The sensor reduction is realized due to the fact that the additional microphones can be used to approximate the pressure gradient at each measurement location to be used for an interpolation of the field.

3 INVESTIGATION OF THE SPATIAL FOURIER TRANSFORM WAVE SEPARATION METHOD FOR USE IN INTERIOR PLANAR FOURIER NEAR-FIELD ACOUSTICAL HOLOGRAPHY

This chapter is a manuscript to be submitted to the Journal of the Acoustical Society of America. The formatting of the paper has been modified to meet the stylistic requirements of this thesis.

3.1 Contributing Authors and Affiliations

Zachary A. Collins
Department of Mechanical Engineering, 435 CTB, Brigham Young University, Provo, UT 84602; email: zcollins26@gmail.com

Kent L. Gee
Department of Physics and Astronomy, N283 ESC, Brigham Young University, Provo, UT 84602; email: kentgee@byu.edu

Scott D. Sommerfeldt
Department of Physics and Astronomy, N283 ESC, Brigham Young University, Provo, UT 84602; email: scott_sommerfeldt@byu.edu

Jonathan D. Blotter
Department of Mechanical Engineering, 435 CTB, Brigham Young University, Provo, UT 84602; email: jblotter@byu.edu

3.2 Abstract

Recent advances in near-field acoustical holography (NAH) have expanded the theory to interior spaces where multiple sources and/or reflections are present. Tamura [*J. Acoust. Soc. Am.* **88**, 2259-2264 (1990)] presented the spatial Fourier transform separation method to measure

the reflection coefficient at oblique angles using two measurement planes in the wave number domain. This paper adapts the spatial Fourier transform separation method for application in interior NAH. A practical exploration of important experimental parameters is performed, which include the relative amplitudes of primary and disturbing sources, the measurement plane separation distance, and an acceptable noise floor. This technique is successfully applied in a reverberant environment to reconstruct the velocity of a clamped vibrating plate.

3.3   Introduction

One of the most restrictive assumptions of the original near-field acoustical holography (NAH) method is that all sources radiate into a free-field and that a reconstruction cannot be obtained on a surface behind any sources.[21]   Unfortunately, many practical situations where noise source identification would be advantageous take place in an enclosed space where reflections are present or in a space where multiple sources are radiating.

Recently, the application of NAH to interior fields or fields with multiple sources has been a research focus. For example, Villot *et al*.[12]   provided a method to perform NAH in a semi-infinite rectangular duct. Kim *et al*.[13] showed that by modifying the original formulation of NAH to include boundary conditions, reflections can be built into NAH reconstructions. Williams *et al*.[14] demonstrated how NAH can be performed inside an aircraft using a combination of NAH and BEM. Jacobsen and Jaud[15] presented the '*p-u method,*' where a simultaneous pressure and normal particle velocity measurement plane allows the contribution of a disturbing source directly opposite the primary source to be negated through an averaging technique. Zhang *et al*.[16] showed a modification of this method where the disturbing source is not required to be symmetric with the primary source. Although it improved the original '*p-u method,*' this technique only provided acceptable results at low frequencies.

In 1990, Tamura[17] presented a method based on spatial Fourier transforms to separate incident and reflected waves and which was first applied to measuring the reflection coefficient of different materials. An experimental verification of this method presented by Tamura *et al.*[18] demonstrated that this technique provided accurate reconstructions up to high angles of incidence, as long as the measurement aperture was large. Cheng[22] applied the spatial Fourier transform separation technique to scattering problems, and investigated the practical application of this technique to a scattered field.[19] He concluded that for best results when scattering is involved, the measurement aperture should be at least three times the diameter of the scatterer, the inter-element spacing should be less than $\lambda/2$, where λ is the wavelength, the technique works better for high frequencies, and the spacing between measurement planes should be less than $3\lambda/16$. Although helpful for certain scenarios, these suggested parameter values do not necessarily apply when the separation technique is applied to NAH.

The spatial Fourier transform technique has been used previously to separate fields for interior NAH, although details of the implementation were not provided.[23,24,25] Others, in their pursuit of other methods, have suggested that Tamura's technique is one possibility for performing interior NAH.[5,26,27,28] Since there has not been a detailed formulation of this technique for NAH, nor a discussion of its usefulness or limitations, this paper provides a derivation of the wave separation method for use with interior Fourier NAH and describes the results of investigations that establish parameters important to implementation. Section II details the theoretical development of the separation method, which modifies the mathematics of Tamura's original implementation that was specific to his application of determining reflection and absorption coefficients. Section III gives a description of the analytical field created for numerical simulations. Section IV uses numerical simulations to investigate the following

11

important parameters: the relative source amplitudes, the plane separation distance, and the signal to noise ratio. Section V provides experimental validation that this technique may be used in a reverberant environment. Section VI states conclusions and recommendations.

3.4 Theory

For interior environments or environments with multiple sources, it is necessary to isolate the sound waves radiating from the sources of interest. For Fourier NAH, all sources of interest must be located behind the reconstruction plane. This becomes problematic for interior NAH problems, since the reflected waves from boundaries of the space can be viewed as coming from virtual interfering sources behind the reconstruction plane. The spatial Fourier transform separation method is convenient to use with NAH because it is based on the same principles: acoustic parameters are propagated to a new plane after taking a two-dimensional Fourier transform of the measured planes of pressure. This separation does not add significant computation because a two-dimensional Fourier transform is already required for NAH to propagate to a separate plane. It should be noted that this separation technique does not completely isolate the radiation coming from the source of interest. The incident portion of the reflection includes waves reflecting or scattering off of the source itself or on some other object behind the source of interest.

The assumption is made that the pressure on a plane is from sources on either side of that measurement plane. For any point in space (using rectangular Cartesian coordinates x, y, and z), the complex pressure can be expressed as

$$p(x, y, z) = p_I(x, y, z) + p_R(x, y, z), \tag{3.1}$$

where p_I and p_R are respectively the incident and reflected portions of the total pressure p.

12

If a two-dimensional spatial Fourier transform is taken over the entire xy plane at the same distance z, the transformed pressure is then expressed as

$$P(k_x, k_y, z) = P_I(k_x, k_y, z) + P_R(k_x, k_y, z),$$
(3.2)

where k_x and k_y are individual wave numbers in the x and y directions, respectively.

In the same manner as performing a propagation from one plane to another in NAH, it is possible to express the transformed pressure on one plane, specified generally as $z = z_i$, as the transformed pressure from another plane, $z = z_j$, multiplied by a propagator function while still in the wave number domain. In this general form, a wave component traveling from $z = z_j$ to $z = z_i$ in the wave number domain is

$$P(k_x, k_y, z_i) = P(k_x, k_y, z_j)e^{ik_z(z_i - z_j)}.$$
(3.3)

For the sake of simplicity, the dependence on k_x and k_y will be assumed for all transformed pressure responses (e.g. $P(k_x, k_y, z_i)$ will be represented as simply $P(z_i)$).

Figure 3-1 is useful in describing the various measurement and reconstruction planes relevant to the application of separating waves coming from multiple sources for use in NAH. Planes $z = z_1$ and $z = z_3$ are the two measurement planes used to separate the incoming and outgoing waves onto $z = z_2$. Using Eq. (3.2) the pressure at the first plane, $z = z_1$, is a combination of incident and reflected waves,

$$P(z_1) = P_I(z_1) + P_R(z_1).$$
(3.4)

The incident and reflected waves can be rewritten according to Eq. (3.3) as wave components propagated from $z = z_2$ to $z = z_1$,

$$P(z_1) = P_I(z_2)e^{ik_z(z_1 - z_2)} + P_R(z_2)e^{-ik_z(z_1 - z_2)}.$$
(3.5)
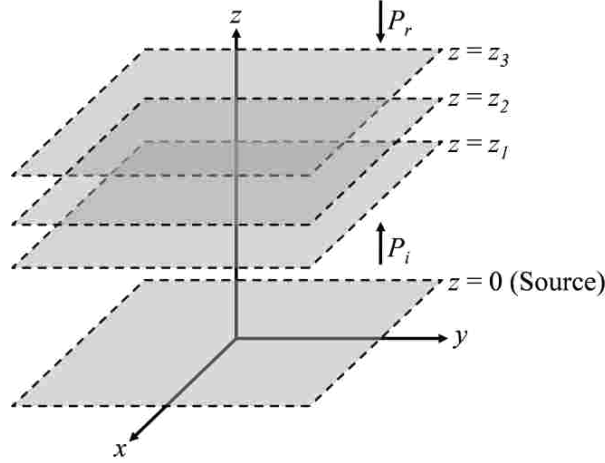
Figure 3-1: The planes required for wave separation. Measurements are made on planes $z = z_1$ and $z = z_3$, then the incident and reflected waves are separated onto plane $z = z_2$.

The same relationship exists between planes $z = z_2$ and $z = z_3$,

$$P(z_3) = P_I(z_2)e^{ik_z(z_3-z_2)} + P_R(z_2)e^{-ik_z(z_3-z_2)}. \tag{3.6}$$

Using Eq. (3.5) and Eq. (3.6) it is possible to solve for the two unknown variables, P_I and P_R at the plane $z = z_2$ since $P(k_x, k_y, z_1)$ and $P(k_x, k_y, z_3)$ will be measured. Solving for P_R from Eq. (3.6) leads to

$$P_R(z_2) = P(z_3)e^{ik_z(z_3-z_2)} - P_I(z_2)e^{2ik_z(z_3-z_2)}. \tag{3.7}$$

Eq. (3.7) is then substituted into Eq. (3.5) and $P_I(z_2)$ is solved for, yielding

$$P_I(z_2) = \frac{P(z_1)-P(z_3)e^{ik_z(z_3-z_2)}e^{-ik_z(z_1-z_2)}}{e^{ik_z(z_1-z_2)}-e^{2ik_z(z_3-z_2)}e^{-ik_z(z_1-z_2)}}, \tag{3.8}$$

where $P_I(z_2)$ is just the incident portion of the waves on the plane $z = z_2$, and it is a function of the measured values $P(z_1)$ and $P(z_3)$. The reflected wave numbers can be solved for by substituting Eq. (3.8) into Eq. (3.7), which results in

$$P_R(z_2) = P(z_3)e^{ik_z(z_3-z_2)} - \left[\frac{P(z_1)-P(z_3)e^{ik_z(z_3-z_2)}e^{-ik_z(z_1-z_2)}}{e^{ik_z(z_1-z_2)}-e^{2ik_z(z_3-z_2)}e^{-ik_z(z_1-z_2)}}\right]e^{2ik_z(z_3-z_2)}. \tag{3.9}$$

14

After the pressure field has been separated at the mid-plane z_2, it is then possible to propagate P_I back to the reconstruction plane using standard Fourier holography processing as if there were no reflections or other disturbing sources present.

3.5   Synthetic Field Creation

In order to test the separation method, a synthetic source was created. A simply supported rectangular plate was chosen as the source for simulations throughout this paper due to the fact that only Cartesian frames are being considered in the present Fourier NAH technique. This source was also chosen because it has a simple closed-form radiation equation. The plate was discretized into point sources and excited by a harmonically driven point source located at (x'_0, y'_0), where the primes indicate coordinates on the plate itself. The plate is also assumed to be surrounded by an infinite, rigid plane baffle. Eq. (3.10), as stated by Willaims,[21] gives the velocity of each point source on the plate as a function of angular frequency, ω.

$$w(x', y', \omega) = -\frac{F}{\rho h} \sum_{m=1}^{\infty} \sum_{n=1}^{\infty} \frac{\Phi_{mn}(x'_0, y'_0) \Phi_{mn}(x', y')}{\omega^2 - \omega_{mn}^2} \tag{3.10}$$

where F is the excitation force amplitude, ρ is the plate material mass per unit area, h is the thickness of the plate, m and n correspond to the number of modes in the x and y direction respectively, ω_{mn} is the eigenfrequency of each mode, and Φ_{mn} is the modal response of the plate given by:

$$\Phi_{mn}(x', y') = \frac{2}{\sqrt{L_x L_y}} \sin\left(\frac{m\pi x'}{L_x}\right) \sin\left(\frac{n\pi y'}{L_y}\right) \tag{3.11}$$

where L_x and L_y are the lengths of the plate in the x and y directions, respectively.

The radiated pressure, shown in Eq. (3.12), can be found by using Rayleigh's integral expressed in terms of the plate displacement to sum up the contributing pressure at any point in

space from each infinitesimal source area element. In these simulations, 441 elements were used for each plate modeled.

$$p(x,y,z,\omega) = -\frac{\omega^2 \rho_0}{2\pi} \int_{-\infty}^{\infty} \int_{-\infty}^{\infty} w(x',y',\omega) \frac{e^{ik|\vec{r}-\vec{r}'|}}{|\vec{r}-\vec{r}'|} dx'dy' \tag{3.12}$$

Figure 3-2 provides a description of the geometric values used in Eq. (3.12). For all simulations in this paper, the plate parameters used are shown in Table 3-I.
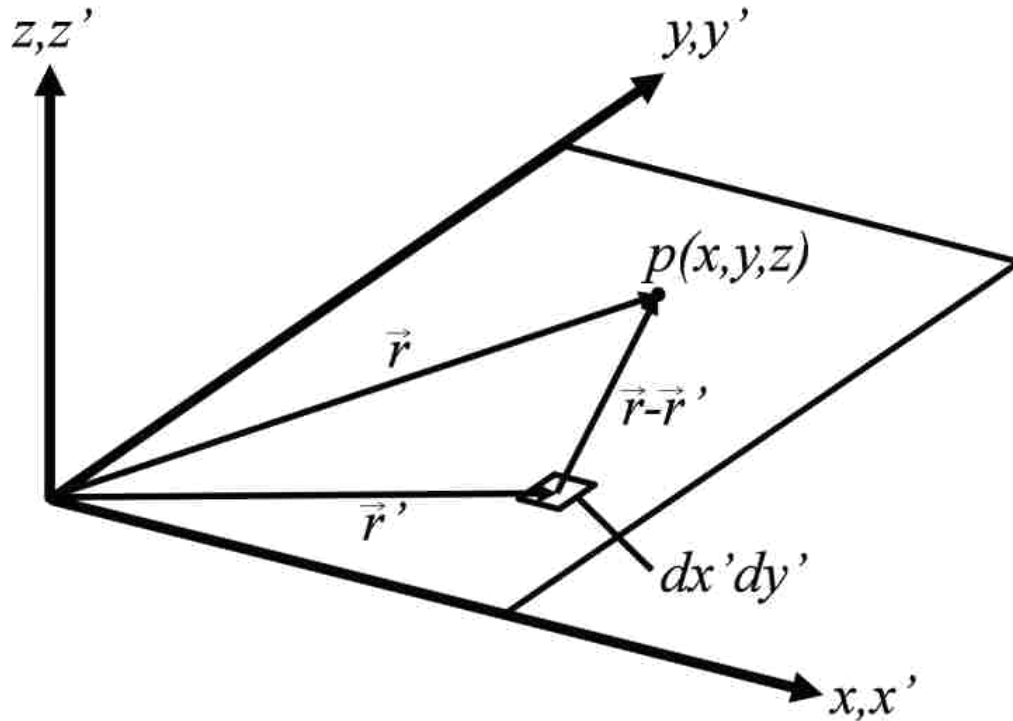
Figure 3-2: A geometric representation of Rayleigh's integral terms

Table 3-1: Analytical Simply-supported Plate Parameters

Parameter	Value
Length, L_x	30.48 (cm)
Width, L_y	45.72 (cm)
Thickness, h	0.3175 (cm)
Material	Aluminum
Density per unit area, ρ	8.5725 (kg/m^2)
Young's Modulus, E	70×10^9 (Pa)
Poisson's Ratio, v	0.35

16

3.5.1 Reflective Wall

Some simulations involve a perfectly reflective wall where the primary reflection is calculated by using a mirrored source on the opposite side of where the wall is located. For example, if the source is located at $z = 0$ cm, and a wall is located at $z = 10$ cm, the primary reflection would be calculated by adding a second, mirrored simply-supported plate located at $z = 20$ cm. For the analytical simulations in this paper, only the primary reflection was calculated.

3.5.2 Error Evaluation

A metric was needed to represent the performance of this separation technique. The chosen metric to evaluate error is a normalized standard deviation, also used by Harris *et al.*[20] This error is computed by first subtracting the separated incident pressure from the actual computed incident pressure at every measurement point, then taking the standard deviation of this error. This standard deviation is computed using the formula,

$$S_e = \sqrt{\frac{1}{N-1} \sum_{i=1}^{n_x} \sum_{j=1}^{n_y} \left[(p - p_{est})_{ij} - \overline{(p - p_{est})_{ij}} \right]^2},$$ (3.13)

where N is the total number of measurement points, n_x and n_y are the number of measurement points in the x and y direction respectively, p is the actual pressure at the point i,j and p_{est} is the reconstructed pressure at the same point. The standard deviation of the errors is then normalized by the maximum absolute measured pressure. This normalized standard deviation of errors is the metric used to measure all errors reported in this paper.

3.5.3 Data Processing

NAH is an inverse problem that can be ill-posed. This is because the solution for the reconstruction is unstable or non-unique because of the finite number of pressure field

measurements, measurement noise, round-off errors, and mainly the presence of evanescent waves. Many errors are introduced as a result of using a finite measurement aperture. The Fourier transform assumes the measurement aperture is infinitely wide in the *x* and *y* directions. However, Fast Fourier Transforms (FFT) that are used for efficient processing of data over a finite aperture repeat the measurement plane and introduce wrap-around error. Additional wave numbers will be introduced into the measurement and, if not filtered out, some unwanted evanescent waves will be propagated back to the source in an exponential manner. For every simulation and experiment, a Tukey window[27] was applied to the measured data and the field was zero-padded to four times the original size, which eliminated some of the high wavenumbers and reduced some of the need for regularization in the processing. A regularization routine was then used to filter out remaining higher wave numbers that are artifacts of the finite measurement aperture.

For regularization, a two-dimensional Harris cosine window has been used.[29]

$$
K_w(k_x, k_y) = \begin{cases} 1 - \dfrac{1}{2} e^{-\left(\left|\sqrt{k_x^2+k_y^2}\right|/k_c\right)/\alpha} & \text{for} \quad \left|\sqrt{k_x^2 + k_y^2}\right| < k_c \\ \dfrac{1}{2} e^{\left(1-\left|\sqrt{k_x^2+k_y^2}\right|/k_c\right)/\alpha} & \text{for} \quad \left|\sqrt{k_x^2 + k_y^2}\right| > k_c \end{cases} \tag{3.14}
$$

Eq. (3.14) shows the wave number filter, K_w, as a function of k_c, the cut-off wave number, and α, which controls the rate of decay of the window. In all simulations, the values of k_c and α were chosen to minimize the standard deviation of the error described above. Due to simplicity of implementation, a non-linear optimization routine that utilizes the Nelder-Mead simplex method of low-dimensions[28] was used to obtain the optimal values of k_c and α.

3.6   Numerical Simulations

A variety of simulations were run using the simply supported plate model described above in order to characterize the performance of the spatial Fourier transform separation technique applied to NAH.   Through exposure to this method, key parameters have been identified that affect the accuracy of the separated fields. The effect of the relative amplitudes of the primary and secondary sources, the distance between measurement planes, and the effect of noise in a measurement were chosen to be investigated in this section. Other effects caused by the spacing between measurement locations,[10] the measurement aperture size,[8] and regularization parameters[29,30] have been investigated previously.

3.6.1   Source Amplitudes

Often, environments where noise identification is needed contain either multiple sources or reflections from the radiating primary source. It was observed through preliminary tests that in some cases, the reflected portion of the separation, P_R, did not always yield an accurate reconstruction. A significant source of error in these separations seemed to be due to the relative amplitudes of the "incident" and "reflected" fields. To investigate this, a numerical simulation was performed using two simply supported plates like those described above. As shown in Figure 3-3, the first plate acted as the primary source. It was located at $z = 0$ cm, had a thickness of 3.175 mm, and was excited at $f = 795.55$ Hz which corresponds to its (3,1) structural mode. A second plate was modeled as the secondary source. It was located at $z = 10$ cm, had a thickness of 5.190 mm, and was excited at the same $f = 795.55$ Hz. Due to the differing plate thicknesses, this corresponds to its (2,2) structural mode. The measurement planes were located at $z_1 = 3.75$ cm and $z_3 = 6.25$ cm, and the separation was made onto a plane at $z_2 = 5$ cm. The incident and reflected portions were then propagated back towards their respective sources. The incident

19

portion was propagated towards the primary source and reconstructed at $z = 0.5$ cm, and the reflected portion was propagated towards the secondary source and reconstructed at $z = 9.5$.cm.
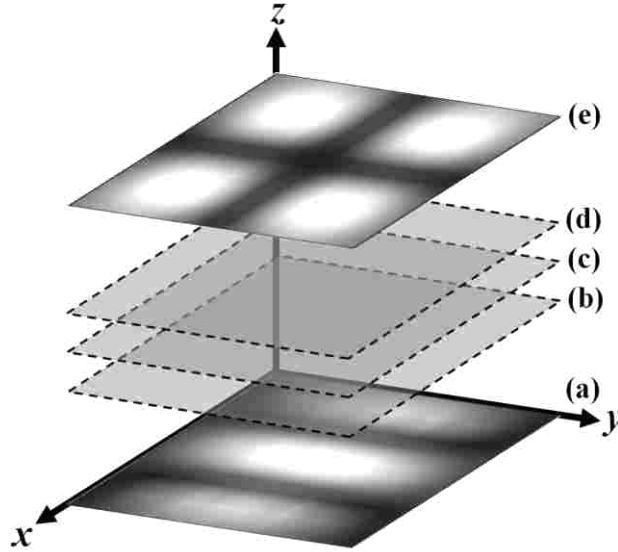
Figure 3-3: A schematic for the numerical simulation exploring the effect of source amplitudes. The primary source was located on plane (a) where $z = 0$ cm, while the secondary source was located on plane (e) where $z = 10$ cm. The pressure was measured on planes (b) and (d), where $z = 3.75$ and $z = 6.25$, respectively. The "incident" and "reflected" portions of the pressure are separated on plane (c), where $z = 5$ cm.

It was observed that for the incident portion to be accurately reconstructed, the maximum pressure amplitude of the primary source must be greater than the maximum pressure amplitude of the secondary source. The parameter μ was used as a ratio of the maximum primary and secondary source amplitudes defined by,

$$\mu = \frac{|P_{max,primary}|}{|P_{max,secondary}|} \tag{3.15}$$

where the maximum pressure of each source was found from points sampled on a plane 0.5 cm from each respective source. The value of μ was then varied between .01 and 100 by changing the excitation force amplitudes, F, for each source. The error was computed for both the primary (incident) pressure reconstruction, and the secondary (reflected) pressure reconstruction for each

value of μ tested. The results are shown in Figure 3-4. The error increased exponentially as the source being reconstructed decreased in power when compared to a disturbing source.
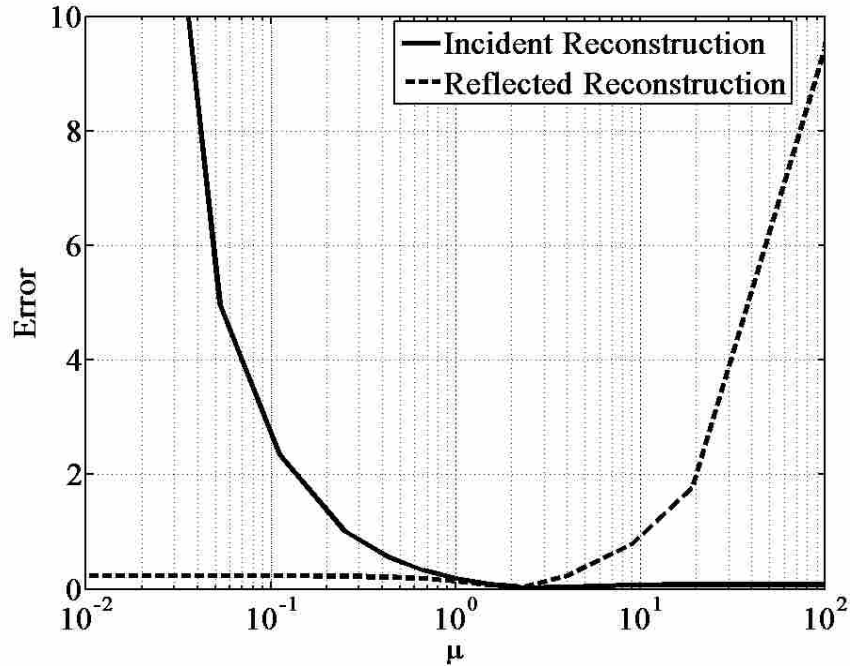
Figure 3-4: The dependence on relative source amplitudes for incident and reflected wave separations. The incident pressure reconstruction becomes more accurate as $\mu > 1$, while the reflected pressure reconstruction becomes more accurate as $\mu < 1$.

As an illustration of the limitations of using this separation method when a disturbing source is present, the incident and reflected reconstructions are shown for three different values of μ. Figures 3-5 (a-c) show the error associated with the reconstructed incident pressure when μ is equal to 0.11, 1.0, and 9.0. The reconstructed incident pressure error decreases as the value of μ increases. As μ exceeds 1, the reconstructed incident pressure begins to match the correct (3,1) mode shape shown as plane (a) in Figure 3-3. Figures 3-6 (d-f) show the reflected pressure reconstructions for the same three values of μ. Here, for values of $\mu \leq 1.0$ the secondary source begins to correspond to the correct (2,2) mode shown as plane (e) in Figure 3-3. It can be concluded that in order to accurately separate the waves coming from two separate sources, the

magnitudes must be nearly equal. If only one source is of interest, that source must be radiating more power than the disturbing source to get an accurate reconstruction.
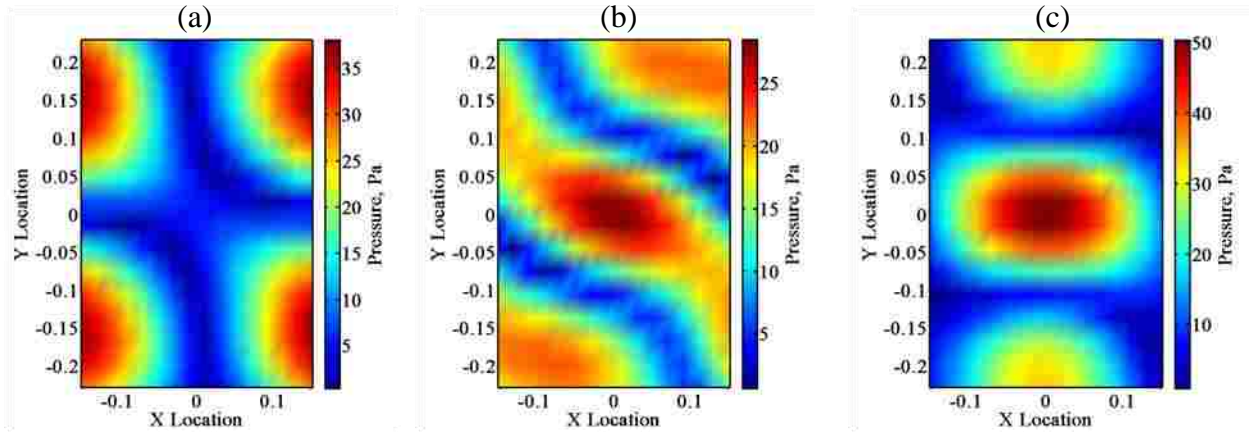
Figure 3-5: The primary source reconstruction from the incident portion of the separated pressure for three values of μ, (a) $\mu = 0.11$, (b) $\mu = 1.0$, (c) $\mu = 9.0$
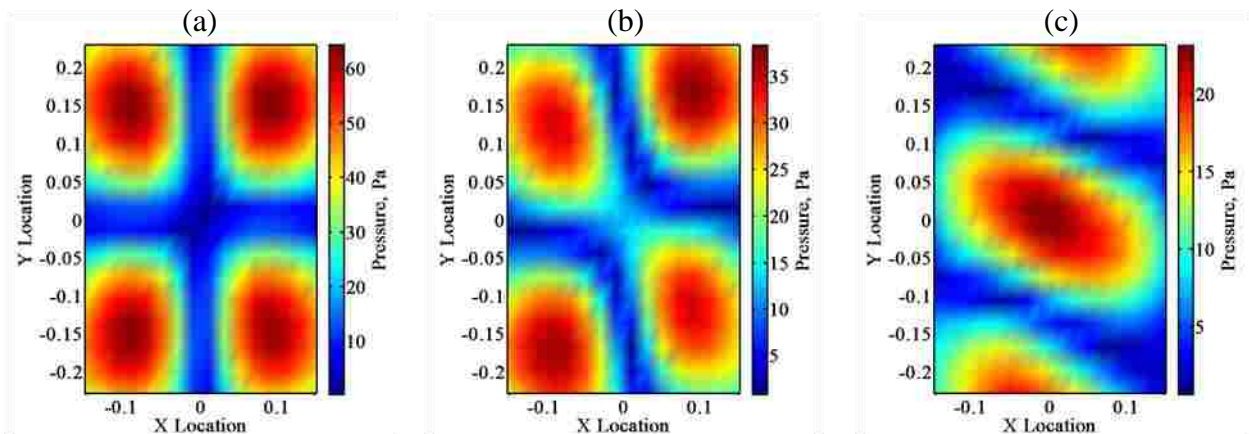
Figure 3-6: The secondary source reconstruction from the reflected portion of the separated pressure for three values of μ, (a) $\mu = 0.11$, (b) $\mu = 1.0$, (c) $\mu = 9.0$

3.6.2 Plane Separation Distance

Another important parameter for a double-planar wave separation is the amount of spacing between measurement planes. In an effort to understand the effect of this plane separation, a simulation was conducted. Using the analytical sound field described above, the pressure was sampled on two measurement planes, the first at $z_1 = 5$ cm from the source, and the

second plane varied based on percentages of the acoustic wavelength, where $z_3 > z_1$. Simulations were run at 487 Hz, 907 Hz, and 1686 Hz. The results are shown in Figure 3-7.
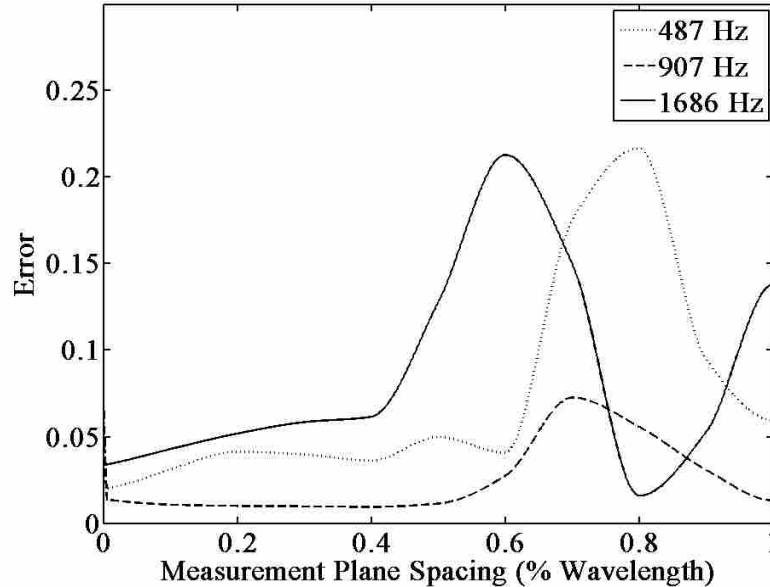
Figure 3-7: The error associated with changing the distance between measurement planes.

It is observed from Figure 3-7 that the error due to changing the measurement plane separation distance is highly dependent on frequency. As the measurement spacing increases, the accuracy of the reconstruction decreases. While the amount of error introduced in the separation is small compared to the error caused by a secondary source being larger in amplitude, the error can be minimized by ensuring the plane separation distance is no greater than 40% of the wavelength of interest. This conclusion is compared to the conclusion given by Cheng[19] that for scattering problems, the separation distance should be kept below $3/16\lambda$. Although the limiting values are different, the same general data trends are observed.

3.6.3 Noise Floor

Experimental measurement in every practical situation includes error from a number of different sources. Error can be added due to microphone positioning, calibration error,

environmental fluctuations, and phase mismatch between microphones. While it is possible to isolate the effects of each source of error, a study was performed which combined all sources of error into a general error. Using the sound field from the simply supported plate described above, a study was completed to find the amount of allowable noise contained in a measurement. The noise strength was varied from 100 dB below the maximum signal, to noise that was equal in amplitude to the signal, where the signal to noise ratio, S/N, is

$$\text{S/N} = 20 \cdot \log_{10}\left(\frac{P_{signal,max}}{P_{noise,max}}\right). \tag{3.16}$$

Figure 3-8 shows the reconstruction error as a function of the signal to noise ratio when the plate was excited at 487 Hz, 907 Hz, and 1686 Hz. It is noticed that the maximum allowable noise before the error rises significantly is dependent upon frequency. This appears to be caused by an increase in spatial variation in the measurement plane at higher frequencies, meaning an increase in the higher wave numbers. The higher spatial frequencies are affected more by the noise and are therefore not able to be reconstructed as well.

3.7   Experimental Validation

3.7.1   Experimental Setup

All simulations up to this point have been computed using either a single primary reflection off a planar wall, or a second source located on the opposite side of the measurement aperture. This technique has not taken into account additional reflections, reflections from side walls, reflections from irregularly shaped walls, or scattering off other objects in the room. To test if this separation technique is still viable in a reverberant enclosure, a physical experiment was performed.

24
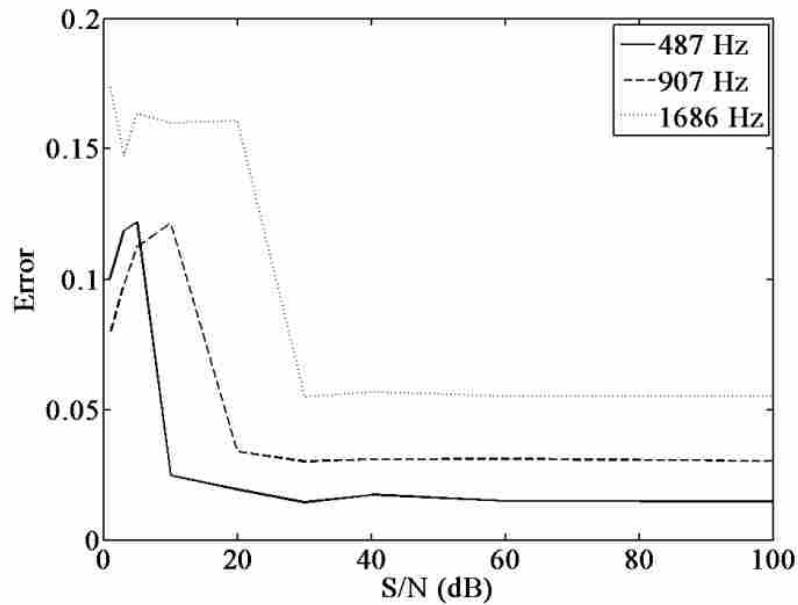
Figure 3-8: The error associated with wave separation when the signal to noise ratio is changed for f = 487, **907, and 1686 Hz.**

A 48.3 cm × 76.2 cm clamped rectangular steel plate was mounted vertically and baffled in a hard rigid wall between two reverberation chambers. The 0.91 mm thick plate was driven by a mechanical shaker located 8.3 cm to the right of the left side of the plate and 62.9 cm above the bottom of the plate. The shaker was driven by a pure 170 Hz sine wave, which excited the (4,3) structural mode of the plate. The plate radiated noise into a 5.70 m × 4.30 m × 2.50 m reverberation chamber with a volume of 61 m^3 and a Schroeder frequency of 552 Hz.

A two-dimensional linear positioning unit, driven by stepper motors, was used to position a six-microphone probe (shown in Figure 3-9). For this experiment, only two of the six microphones were used. The microphones were G.R.A.S. 40GI 12.7 mm (0.5 in) phase-matched microphone pairs, powered by G.R.A.S 26CB CCP preamplifiers. The closest microphone took measurements on the plane $z_1 = 13$ cm, while the further microphone sampled the field along the plane $z_3 = 18$ cm. The linear positioning unit was controlled by a program written in LabVIEW which simultaneously recorded the pressure measurements from each microphone at each chosen

25

location. An area four times the size of the plate, twice the length and width, was sampled at 5 kHz. The distance between measurement locations in the x-direction was given by $\Delta x = 7.86$ cm while the separation in the y-direction was given by $\Delta y = 11.43$ cm. A reference microphone was used to obtain the correct source phase for each microphone location.

Figure 3-9: The experimental setup showing the scanning system in front of a clamped rectangular plate mounted inside a reverberation chamber.

As a reconstruction benchmark, a Polytec 400V scanning laser Doppler vibrometer (SLDV) was used to measure the velocity response of the plate when excited. A single frequency scan was performed at 170 Hz. SLDV scans were taken before and after each experimental test. Although the plate response did not change significantly, the average of these two scans was used to compare the normal particle velocity reconstruction from NAH. The normal particle velocity was able to be reconstructed from the pressure hologram by modifying the propagator function as described by Williams.[1]

The data processing included applying a twenty-point Tukey window to the measured data, zero-padding the data to four times the measurement aperture, and using the same regularization routine described for the numerical simulations of the simply supported plate above.

3.7.2 Experimental Results

The sampled pressure from measurement planes $z_1 = 13$ cm and $z_3 = 18$ cm are shown in Figure 3-10.
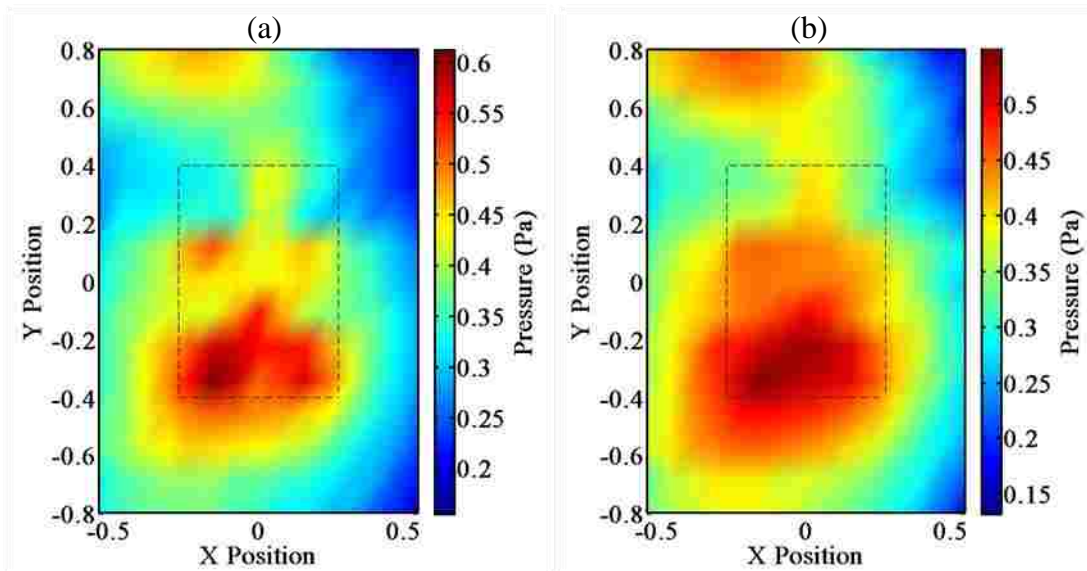
Figure 3-10: Measured pressure at (a) the $z_1 = 13$ cm plane, and (b) the $z_3 = 18$ cm plane. The dotted rectangular line represents the area where the vibrating plate is located.

Using these two measurement planes, the normal particle velocity can be reconstructed at the surface of the plate. Figure 3-11 shows the resulting reconstructed velocity with and without using the spatial Fourier transform separation method and a comparison with the SLDV velocity measurements. Even in a reverberant environment with a modal acoustic field, the separation method was able to separate the incident waves from the reflected waves. Comparing Figure 3-

11(a) with Figure 3-11(b), it can be seen that the separation method correctly reconstructs the velocity response of the vibrating plate, while no such agreement can be discerned when the separation technique is not used in Figure 3-11(c). Thus, by using the separation technique, reconstruction results that are similar to results for free-field reconstruction can be achieved.
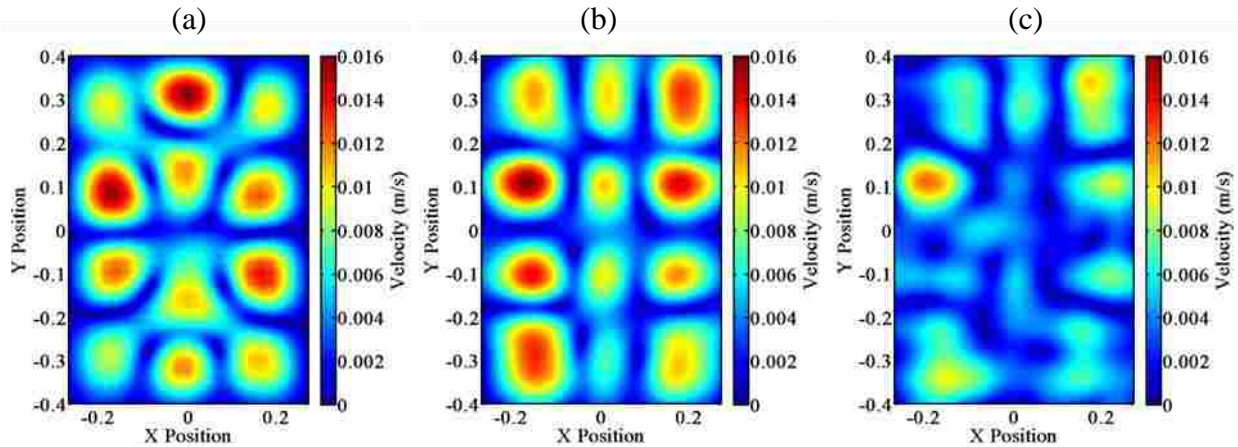
Figure 3-4: Experimental results (a) the measured velocity of the plate, (b) the reconstructed velocity after being separated, and (c) the reconstructed velocity without performing a separation.

3.8   Conclusion

The spatial Fourier transform method of wave separation provides a useful technique for performing interior NAH. This separation method has been adapted for the use of performing NAH, and results from analytical simulations as well as a physical experiment in a reverberant environment are shown. This method is simple to incorporate into free-field Fourier NAH code and does not significantly add to the computational expense. Guidelines have been developed for its use when multiple sources are present.

In order to correctly isolate and reconstruct the waves coming from one side of the measurement aperture, the radiated pressure from that side must be equal to or greater than any radiated pressure entering the measurement aperture from the opposite side. In other words, the

28

noise coming from a disturbing source must not be greater than the pressure due to the source of interest.

For an accurate separation, the measurement planes should be closely spaced. Simulations showed that for best results, the measurement planes should be spaced no more than 40% of the acoustic wavelength from each other.

The amount of allowable noise in a measurement is dependent on the spatial distribution of pressure. Large spatial variation requires a larger signal to noise ratio. For some cases, the signal to noise ratio must be at least 30 dB.

There are many opportunities to conduct further research in the area of interior NAH. It would be beneficial to further isolate the source of interest by separating any reflected or scattered waves from the incident pressure separation. This would allow more accurate reconstructions to take place. It would also be beneficial to isolate the effects of measurement position error, microphone phase mismatch, and microphone calibration error on the separated field.

3.9   Acknowledgments

4 DATA INTERPOLATION METHODS FOR OBTAINING THE COMPLEX PRESSURE FIELD FOR INTERIOR NEAR-FIELD ACOUSTICAL HOLOGRAPHY

This chapter presents a manuscript to be submitted to the Journal of the Acoustical Society of America. The formatting of the paper has been modified to meet the stylistic requirements of this thesis.

4.1 Contributing Authors

Zachary A. Collins
Department of Mechanical Engineering, 435 CTB, Brigham Young University, Provo, UT 84602; email: zcollins26@gmail.com

Kent L. Gee
Department of Physics and Astronomy, N283 ESC, Brigham Young University, Provo, UT 84602; email: kentgee@byu.edu

Scott D. Sommerfeldt
Department of Physics and Astronomy, N283 ESC, Brigham Young University, Provo, UT 84602; email: scott_sommerfeldt@byu.edu

Jonathan D. Blotter
Department of Mechanical Engineering, 435 CTB, Brigham Young University, Provo, UT 84602; email: jblotter@byu.edu

4.2 Abstract

Near-field acoustical holography (NAH) methods based on the measurement of pressure and particle velocity have led to the ability to reduce the required measurement locations. Other recent advances in NAH have expanded the theory to interior spaces where multiple sources and/or reflections are present. This paper investigates the use of interpolation techniques to

reduce the required measurement locations for interior NAH. Specifically, the benefits of a bi-cubic Hermite surface patch interpolation are discussed and compared to other interpolation routines. Although the required inputs for the Hermite interpolation can be measured using a variety of devices, a scanning six-microphone probe in a tetrahedral configuration is suggested. The six microphones are utilized to simultaneously sample pressure on two parallel planes and estimate the pressure gradients on both of these planes. The two interpolated measurement holograms are used to separate the incoming and outgoing waves using the spatial Fourier-transform method. Analytical simulations of simply supported plates are shown as well as experimental results in a reverberation room to characterize the reduction in measurement locations. Depending on the spatial frequency of the hologram, a measurement location reduction of 20–80% was observed.

4.3   Introduction

One of the most restrictive assumptions of the original NAH method is that all sources must radiate into a free-field and that a reconstruction cannot be obtained on a surface behind any sources. Unfortunately, many practical situations where noise source identification would be advantageous take place in an enclosed space where reflections are present or in a space where multiple sources are radiating.

Recently, the application of NAH has been expanded to interior fields or fields with multiple sources. Gardner and Bernhard were the first to apply NAH to an interior field.[31] They used the inverse boundary element method (IBEM) to show the interaction between acoustic sources and points within the interior field or surface. Villot, et al.[12] provided a method to perform NAH in a semi-infinite rectangular duct. Kim, et al.[13] showed that by modifying the original formulation of NAH to include boundary conditions, reflections can be built into NAH

reconstructions. Williams, et al.[14] demonstrated how NAH can be performed inside an aircraft using a combination of NAH and BEM. Jacobsen and Jaud[15] presented the '*p-u method*,' where a simultaneous pressure and normal particle velocity measurement plane allows the contribution of a disturbing source directly opposite the primary source to be negated through an averaging technique. Zhang, et al.[16] showed a modification of this method where the disturbing source is not required to be symmetric with the primary source. Although it improved the original '*p-u method*,' this technique only provided descent results at low frequencies.

Many interior NAH methods require measurements on two separate measurement planes to help distinguish between sounds coming from each side of the measurement plane.[17,32] When a large amount of pressure measurements are needed to create accurate holograms, the number of measurement locations are often unreasonable, or too costly. This paper discusses the use of a commercial six-microphone probe in a tetrahedral formation to simultaneously measure the pressure on both measurement planes, as well as provide an estimate of the pressure gradients to be used for interpolation.

Harris, et al.[20] were able to show that the number of sensors required to create an adequate hologram can be reduced by measuring the pressure and particle velocity at each location, then using an interpolation scheme to effectively increase the measurement density. The measured particle velocity is used to estimate the pressure gradient which is then used to create a bi-cubic Hermite surface interpolation patch between each measurement point. This pressure field interpolation was shown to reduce the number of measurement locations by up to 70%.

This paper explains how by using this same interpolation method, the number of required measurement locations can be reduced through the use of a probe with multiple microphones.

The sensor reduction is realized due to the fact that the additional microphones can be used to approximate the pressure gradient at each measurement location to be used for an interpolation of the field.

4.4   Theoretical Formulation

4.4.1   Synthetic Field Creation

Throughout this paper, several numerical simulations are performed.   For these simulations, the pressure field was calculated using an analytical form of a simply supported plate. The error metric used was the normalized standard deviation of errors, shown in Eq. (4.1). Both the field creation and error metric were described by Collins, et al.[33]

$$S_e = \sqrt{\frac{1}{N-1} \sum_{i=1}^{n_x} \sum_{j=1}^{n_y} \left[(p - p_{est})_{ij} - \overline{(p - p_{est})_{ij}} \right]^2} \qquad (4.1)$$

4.4.2   Bi-cubic Hermite Surface Patch Interpolation

There are several methods to determine the measurement spacing needed for proper reconstruction. Maynard suggested that the spacing between measurements should be less than or equal to d, where d is the distance from the source to the measurement plane.[34] Williams stated that the required measurement spacing depends on the distance to the source and the signal to noise ratio.[21] He quantified this recommendation according to

$$d < \frac{(R_x D)}{20\pi \log e}, \qquad (4.2)$$

where R_x is the desired spatial resolution, d is the distance from the source, and D is the signal to noise ratio.

Harris, et al. showed that these suggestions for measurement spacing can be increased by interpolating the measurement hologram. They showed that the number of sensor locations required for an NAH reconstruction can be reduced by up to 70% through the use of simultaneous pressure and estimates of the derivative of the pressure to create a bi-cubic Hermite interpolation.[20]

If the pressure and the gradient of the pressure are known on a two dimensional grid, an interpolated surface can be solved for that closely matches the actual pressure contours. This interpolated surface is found by breaking up the measurement aperture into patches composed of the space between four pressure measurements. The interpolation is done in parameter space illustrated in Figure 4-1. The mapping from real space (x,y) to parameter space (r,s) is done by

$$r = \frac{x-x_0}{\Delta x},$$
$$s = \frac{y-y_0}{\Delta y},$$

(4.3)

where Δx and Δy are the respective distances between measurement points in the x and y directions. The pressure gradients must also be mapped into parameter space using

$$\boldsymbol{f}^r = \frac{\partial \boldsymbol{f}}{\partial x} \cdot \frac{\Delta x}{\Delta r},$$
$$\boldsymbol{f}^s = \frac{\partial \boldsymbol{f}}{\partial y} \cdot \frac{\Delta y}{\Delta r},$$

(4.4)

where Δr and Δs are equal to one because they are restricted to vary from 0 to 1. Then using the values of the pressure, $\boldsymbol{f}$, and x and y pressure gradients, $\boldsymbol{f}^r$ and $\boldsymbol{f}^s$ respectively at each corner, a cubic Hermite curve is created that bounds each of the four sides of the patch.

The conventional geometric form of this interpolation is given by:

$$\mathbf{f}(r,s) = \mathbf{R}\mathbf{M}_H\mathbf{G}_H\mathbf{M}_H\mathbf{S}^T$$

(4.5)

where $\mathbf{R} = [r^3 \ r^2 \ r \ 1], \mathbf{S} = [s^3 \ s^2 \ s \ 1]$, and $\mathbf{M}_H$ is the Hermite basis transformation matrix,

$$M_H = \begin{bmatrix} 2 & -2 & 1 & 1 \\ -3 & 3 & -2 & -1 \\ 0 & 0 & 1 & 0 \\ 1 & 0 & 0 & 0 \end{bmatrix}. \tag{4.6}$$
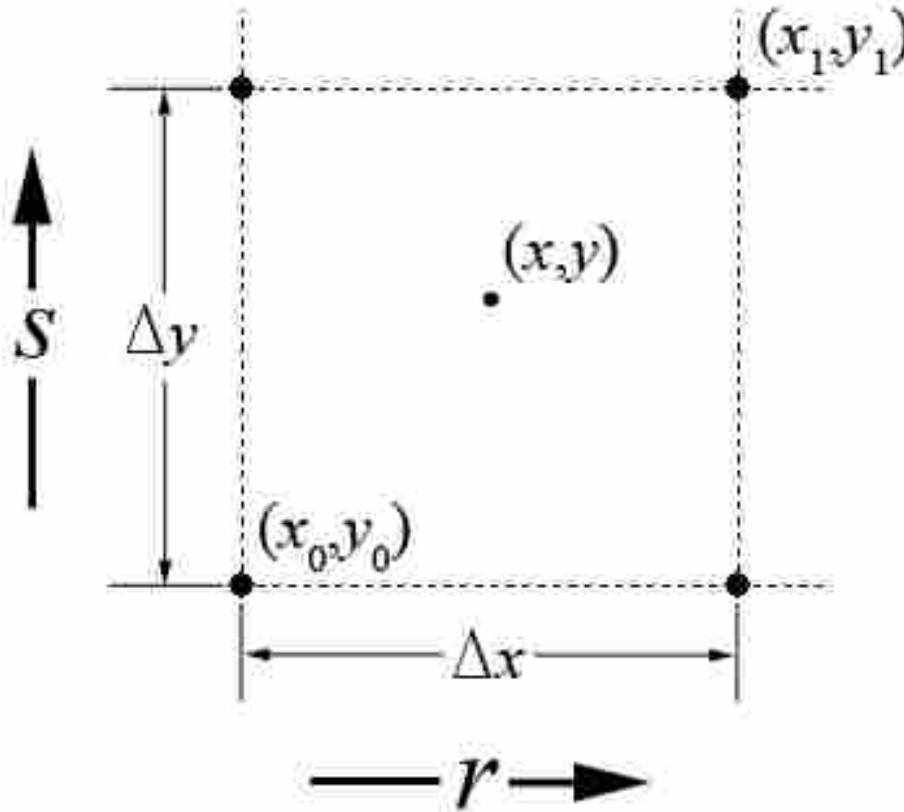
Figure 4-1: A geometric representation of the mapping between real and parameter space

G_H is composed of the patch's corner pressures and corresponding derivatives of pressure,

$$G_H = \begin{bmatrix} f_{00} & f_{01} & f_{00}^s & f_{01}^s \\ f_{10} & f_{11} & f_{10}^s & f_{11}^s \\ f_{00}^r & f_{01}^r & f_{00}^{rs} & f_{01}^{rs} \\ f_{10}^r & f_{11}^r & f_{10}^{rs} & f_{11}^{rs} \end{bmatrix} \tag{4.7}$$

where the values in this matrix are shown in Figure 4-2. The subscripts indicate the location of

the input, while the superscripts denote what the derivative is taken with respect to.
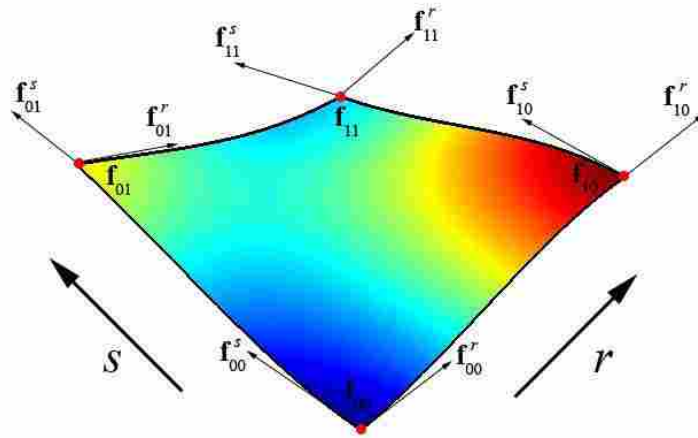
Figure 4-2: A single Hermite patch with required inputs

Once the interpolation for the patch is complete, the values can be mapped back to real space and the process is repeated for every patch resulting in a continuous interpolation where the pressure values and their derivatives match at the corners of every patch.

Interpolation Comparison: As a benchmark for the benefit of using this technique, free-field simulations were run to compare the bi-cubic Hermite interpolation with three other cases: no interpolation, linear interpolation between pressure measurements, and a cubic spline interpolation between points that doesn't rely on the pressure gradient.

For this simulation, the analytical field described in the previous section was used. The pressure was calculated on a plane 5 cm from the source, the field was interpolated with the given treatment, zero-padded to twice the x and y dimensions, propagated back to a plane 2 cm from the source, regularized, then compared to the actual pressure on a plane 2 cm from the source. The error was calculated by the formula described above. A number of measurement densities were explored, from a 4×4 microphone grid to a 28×28 microphone grid. Figure 4-3 shows the error associated with each interpolation technique as a function of the number of sensors used in the x and y directions for two different frequencies. Using Maynard's technique

described above to determine the measurement spacing, the microphones should sample the space at least every 5 cm since the measurement aperture is 5 cm from the source. This corresponds to 19 sensors in Figure 4-3, which can be seen as an acceptable measurement spacing no matter which interpolation technique is used. It can be noted that when using the bi-cubic Hermite surface patch interpolation, the measurement spacing can be increased while the amount of error remains the same. It is also noted that the benefit of using this interpolation technique varies slightly depending on the source frequency and the spatial frequency of the hologram. For every case, the proposed Hermite interpolation performed better than every other interpolation technique, while the linear interpolation never consistently provided any benefit. This comparison between interpolation methods gives a foundation for using the bi-cubic Hermite surface patch interpolation when two parallel measurement planes are used. For the remaining simulations discussed in this paper, the linear interpolation method was not investigated due to its poor performance.

(a)   (b)
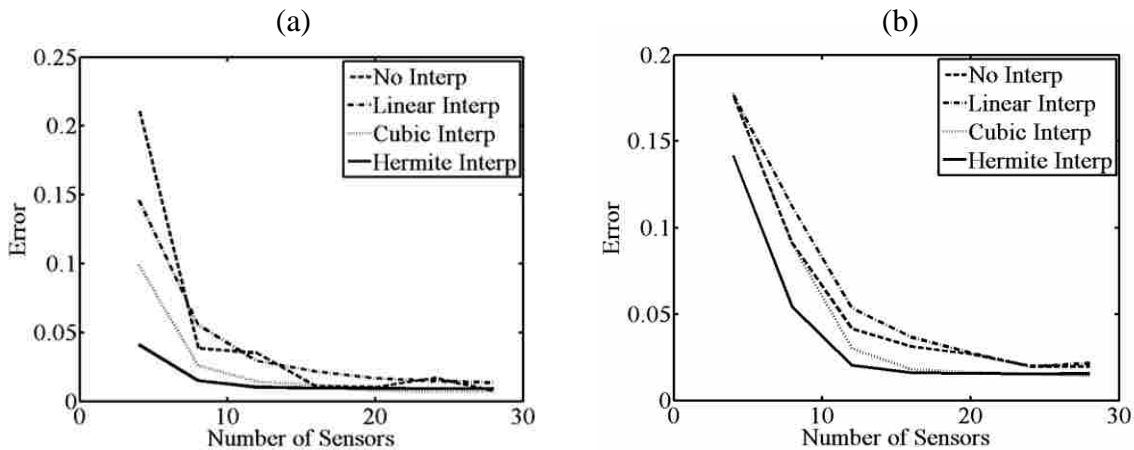
Figure 4-3: A comparison of interpolation techniques based on the number of sensors when the source is excited at (a) 374 Hz and (b) 907 Hz

To understand what effect noise plays in using a finite-difference approximation to compute the pressure gradients, another simulation was run using the analytical field from the

simply supported plate described above. The field was sampled at a plane 5 cm from the source

and the pressure gradients were estimated on the same plane. The noise strength was varied

from 60 dB below the max signal to noise that was equal in amplitude to the signal. The spacing

between the sensors computing the pressure gradient was also varied from 0 to 10 cm. Figure 4-

4 shows that significant error does not occur until the signal to noise ratio is below 20 dB. If the

signal to noise ratio is less than this, a larger sensor spacing can be used to reduce the error, but

this will also decrease the ability of the interpolation routine to accurately interpolate fields with

high spatial frequency.
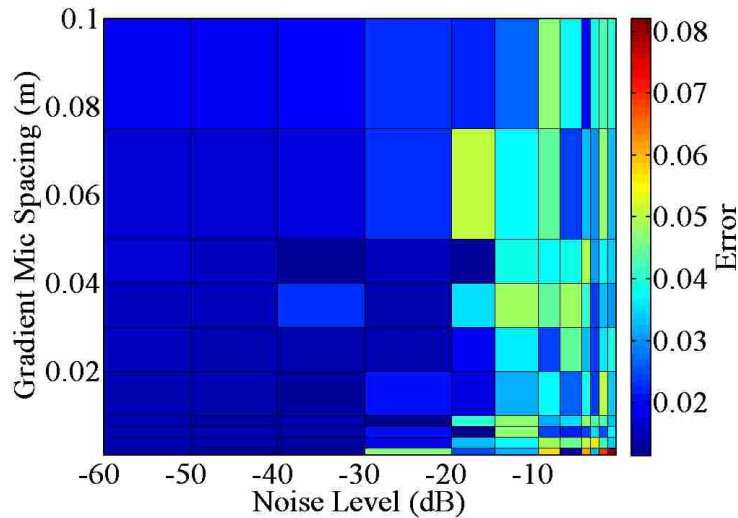
Figure 4-4: The error associated with varying the microphone spacing and the noise floor

Double Planar Hologram Measurement: For a double planar technique, two

measurement planes must be interpolated. This can be done in a variety of ways. To perform

the bi-cubic Hermite interpolation, the collocated pressure and in-plane pressure gradients must

be measured for each plane. One implementation to obtain these measurements is to use a six-

microphone probe to perform a simultaneous pressure measurement on two planes as well as an

estimate of the pressure gradient on each of those two planes. Figure 4-5 shows a diagram of the

six-microphone probe suggested. Each pair of microphones, A and B, C and D, E and F, are

separated by a distance δ Microphones A and B would respectively measure the pressure on planes $z = z_3$ and $z = z_1$, while the four microphones on plane $z = z_2$ would be used to estimate the gradients for both planes $z = z_1$ and $z = z_3$. The gradients are calculated by using Eq. (4.8) and Eq. (4.9).

$$dPdx = \frac{P_D - P_C}{\delta} \qquad (4.8)$$

$$dPdy = \frac{P_F - P_E}{\delta} \qquad (4.9)$$
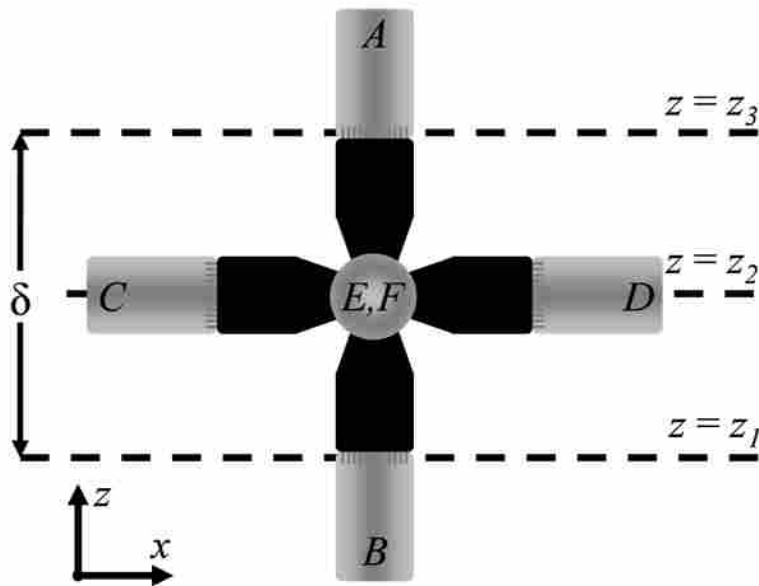
Figure 4-5: A six-microphone probe in a tetrahedral configuration.

Using a mid-plane to estimate the gradients will introduce additional error, but this error was found to be insignificant as long as the gradients are estimated on a plane close to the intended plane of use. Using the same analytical field described above, the gradients were estimated on planes varying from 4 cm closer to the source to 4 cm away from the source. The plate was excited at 100 Hz, 200Hz, and 400Hz while the distance from the source, D, was varied from 5 to 6 cm. The results are shown in Figure 4-6.
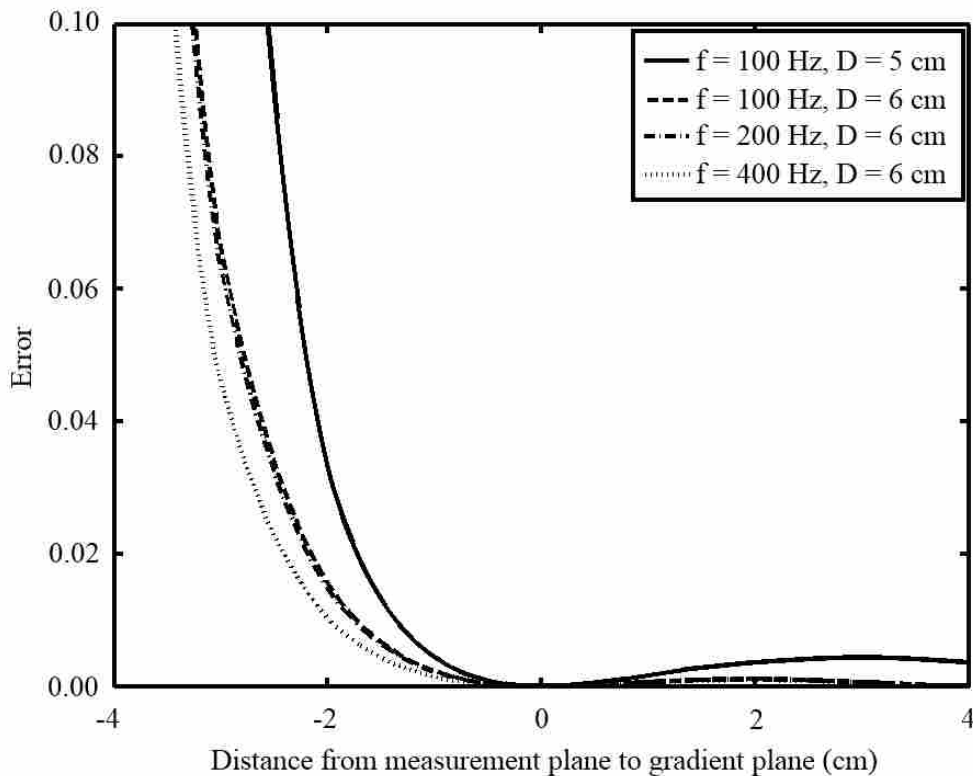
Figure 4-6: Error associated with using a separate plane to estimate the pressure gradient. The distance from the measurement plane to the gradient plane is defined as $z_2 - z_1$ where z_1 and z_2 are the distances from the source to the measurement plane and plane where the gradients are estimated, respectively.

4.4.3 Wave Separation

For interior environments or environments with multiple sources, it is necessary to isolate the sound waves radiating from the sources of interest. For Fourier NAH, all sources of interest must be located behind the reconstruction plane, and any reconstruction cannot extend past the surface of any source. To isolate the sound waves coming from one side of the measurement planes, the spatial Fourier transform separation method was utilized. This method, originally developed by Tamura, et al.[18] as a method of computing reflection coefficients at oblique angles, was adapted for use in interior NAH by Collins, et al.[33] Figure 4-7 shows a schematic of the planes involved for this separation method. The pressure is measured on the planes $z = z_1$ and $z = z_3$, then separated onto the plane $z = z_2$.
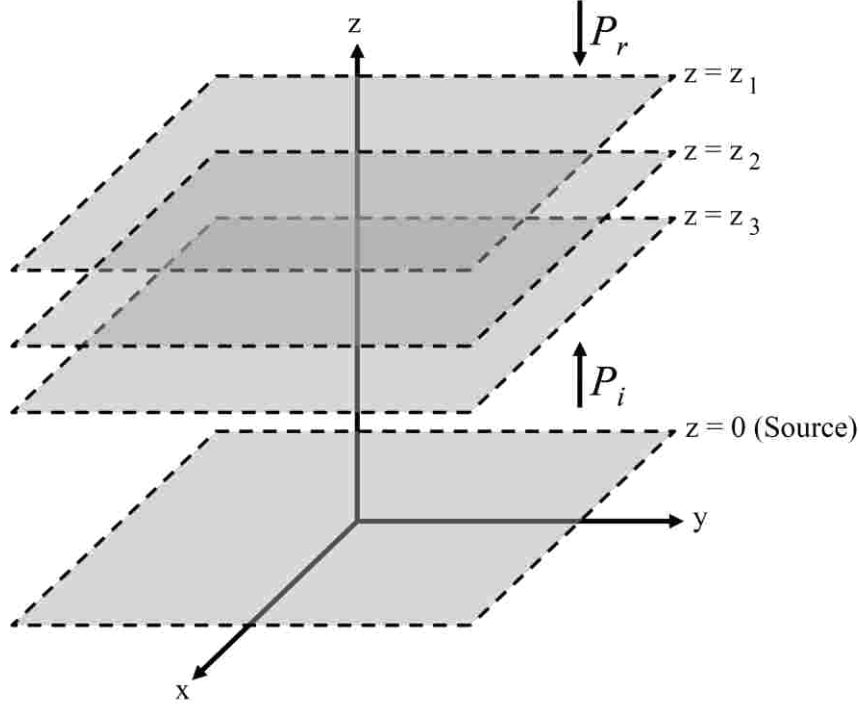
Figure 4-7: The planes used for spatial Fourier transform wave separation method

The incident portion of the separated pressure in the wave number domain is,

$$P_i(k_x, k_y, z_2) = \frac{P(k_x,k_y,z_1) - P(k_x,k_y,z_3)e^{ik_z(z_3-z_2)}e^{-ik_z(z_1-z_2)}}{e^{ik_z(z_1-z_2)} - e^{2ik_z(z_3-z_2)}e^{-ik_z(z_1-z_2)}}, \tag{4.10}$$

where $P(k_x, k_y, z_1)$ is the measured pressure on the plane $z = z_1$, and is a function of k_x and k_y, the wave numbers in the x and y-directions, $P(k_x, k_y, z_3)$ is the measured pressure on the plane $z = z_3$, and k_z is the wave number in the z direction. A similar equation for the reflected portion of the separated pressure is given in Eq. (4.11).

$$P_r(k_x, k_y, z_2) = P(k_x, k_y, z_3)e^{ik_z(z_3-z_2)}$$
$$- \left[\frac{P(k_x, k_y, z_1) - P(k_x, k_y, z_3)e^{ik_z(z_3-z_2)}e^{-ik_z(z_1-z_2)}}{e^{ik_z(z_1-z_2)} - e^{2ik_z(z_3-z_2)}e^{-ik_z(z_1-z_2)}} \right] e^{2ik_z(z_3-z_2)}. \tag{4.11}$$

After the pressure field has been separated onto the mid-plane z_2, it is then possible to propagate back to the reconstruction plane as if there were no reflections or disturbing sources present.

4.5   Numerical Simulation

To illustrate the entire process, the analytical simply supported plate described above was used with a reflective wall located at z_{wall} = 11 cm to simulate a sound field. The plate was excited at an arbitrary frequency given by f = 921 Hz. Figure 4-8 shows the velocity field 2 cm from a simply supported plate when excited at 921 Hz.
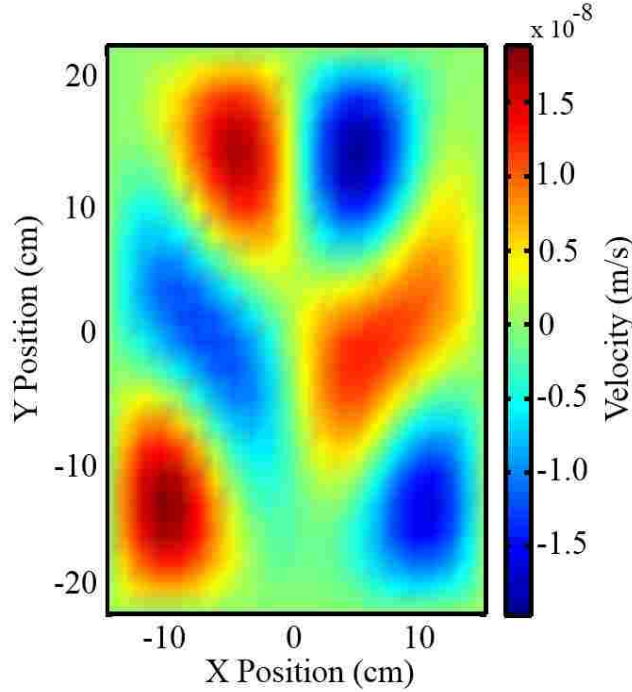
Figure 4-8: Velocity response of analytical plate excited at 921 Hz

The pressure field radiating from this plate was calculated on three planes, as if a six-microphone probe were used to measure the pressure, with z_1 = 5 cm, z_2 = 7.5 cm, and z_3 = 10 cm. Therefore, δ = 5 cm for this probe. Once the pressure was interpolated on the planes $z = z_1$ and $z = z_3$, the incident waves were separated from the reflected waves and the velocity was reconstructed on a plane 2 cm from the source. The error was calculated as described above.

To show the theoretical benefit of using the bi-cubic Hermite surface patch interpolation, the number of sensors used to sample the field was varied in the x and y direction. The results are compared to two benchmarks. The first is performing the separation and propagation without

using any field interpolation, and the second is after performing a cubic spline interpolation (without the use of the mid-plane gradient approximations). The error was plotted for each combination of sensors used and is shown in Figure 4-9.
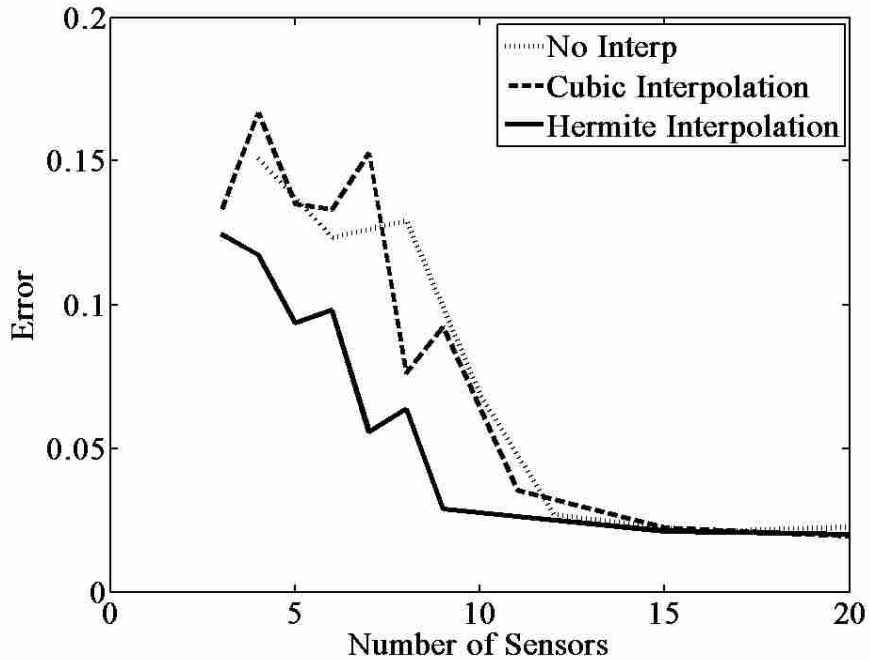
Figure 4-9: A comparison of the errors associated with different interpolation techniques.

The recommended measurement spacing according to Maynard's criterion is 5 cm which corresponds to 19 sensors in each direction. The proposed bi-cubic Hermite interpolation allows the same amount of error when 9 sensors are used in each direction. This corresponds to about a 78% reduction in sensor positions from the suggested number of sensors. Since the field was sampled at a number of different sensor densities, it was possible to observe that at this frequency, the field could have been sampled with a 12×12 array without any interpolation and still produce as accurate of a reconstruction. This corresponds to a sensor reduction count of about 44%.

As an illustrative point, when a 9×9 measurement array is used to sample the field, Figure 4-10 shows the actual pressure at the $z = 2$ cm plane. The reconstructed pressure obtained after

using the Hermite interpolation is shown in Figure 4-11 and the reconstructed pressure obtained

after using a cubic spline interpolation is shown in Figure 4-12.
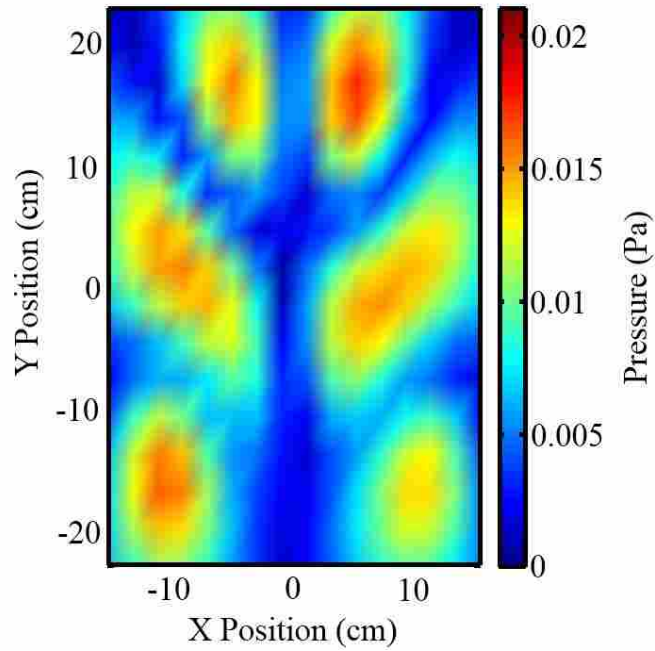
Figure 4-10: The actual pressure at the plane z = 2 cm.
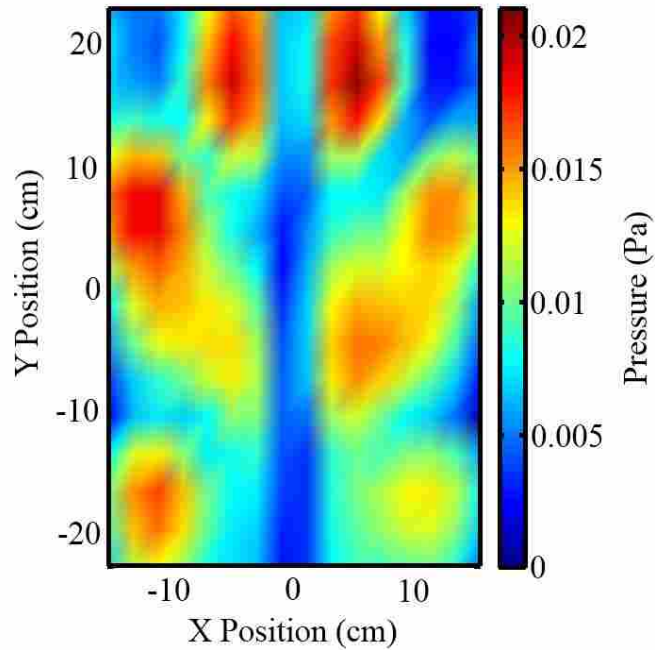
Figure 4-11: The reconstructed pressure when a 9x9 microphone array is used with Hermite interpolation.
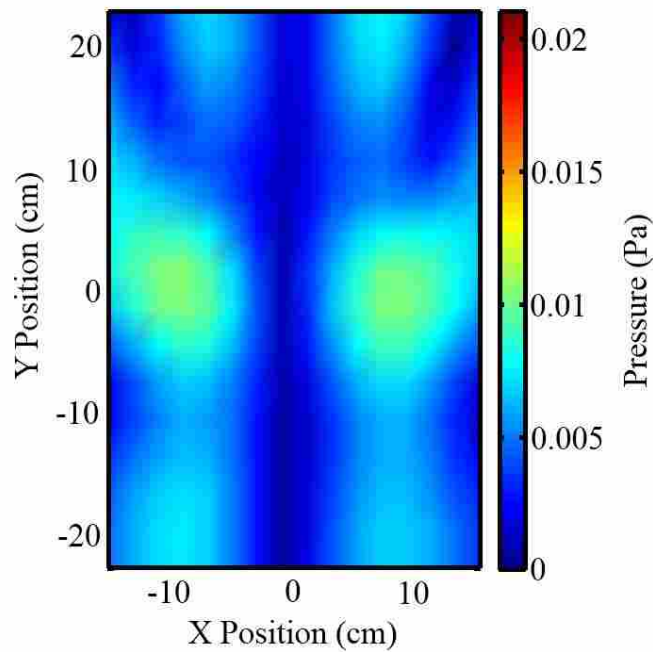
Figure 4-12: The reconstruction pressure when a 9x9 microphone array is used with a cubic spline interpolation.

As expected, the sensor reduction benefit was highly dependent upon the spatial frequency of the measurement field. The proposed bi-cubic Hermite interpolation method using a six microphone probe consistently provided the least amount of error regardless of the frequency of interest. When the field was interpolated using cubic splines without the use of measured pressure gradients, the reconstructions were at least as good as when no interpolation was used, but occasionally performed just as well as when the bi-cubic Hermite interpolation was used. For all frequencies tested, the sensor reduction varied from 20% to 80% depending on the spatial pressure contours.

4.6 Experimentation Validation

4.6.1 Experimental Setup

A 48.3 cm × 76.2 cm clamped rectangular steel plate was mounted vertically in a wall so as to baffle the plate. The 0.91 mm thick plate was driven by a mechanical shaker located 8.3 cm to the right of the left wall and 62.9 cm above the bottom of the plate. The shaker was driven by a pure 170 Hz sine wave which excited the (4,3) structural mode of the plate. The plate radiated noise into a 5.70 m × 4.30 m × 2.50 m reverberation chamber with a volume of 61 m^3 and a Schroeder frequency of 552 Hz.

Figure 4-13: The experimental setup

A two-dimensional linear positioning unit, driven by stepper motors, was used to position a six-microphone probe (shown in Figure 4-13). The six-microphone probe was composed of three sets of G.R.A.S. 40GI ½" phase-matched microphone pairs, powered by G.R.A.S 26CB CCP preamplifiers. For this probe, δ was 5cm. The linear positioning unit was controlled by a program written in LabVIEW which simultaneously recorded the pressure measurements from each microphone at each chosen location. An area four times the size of the plate was sampled

at 5 kHz. A variety of measurement spacings were used to sample the field ranging from 3×3 point measurement arrays to 21×21 point measurement arrays. This provided a means of computing a sensor reduction when compared to other interpolation techniques. The recorded pressures at each location were phase-locked by using a reference microphone.

As a reconstruction benchmark, a scanning laser Doppler vibrometer (SLDV) was used to measure the velocity response of the plate when excited. SLDV scans were taken before and after each experimental test. Although the plate response didn't change significantly, the average of these two scans was used to compare the normal particle velocity reconstruction from NAH. The normal particle velocity was able to be reconstructed from the pressure hologram by modifying the propagator function. The angular spectrum components of normal velocity in one plane are related to the spectral components of pressure in a different plane by:[21]

$$\dot{W}(k_x, k_y, z_k) = \frac{k_z}{\rho_0 ck} P(k_x, k_y, z_j) e^{ik_z(z_k - z_j)}, \tag{4.12}$$

where the pressure from the plane $z = z_j$ is being propagated to the normal velocity on plane $z = z_k$, ρ_0 is the density of air, c is the speed of sound in air, k is the wave number of interest, and k_x, k_y, and k_z are the wave numbers in the x, y, and z-directions, respectively.

The data processing included applying a Tukey window to the measured data, zero-padding the data to four times the measurement aperture, and using the same regularization routine described by Collins.[33]

4.6.2   Experimental Results

The averaged velocity scans of the plate, used for the reconstruction benchmark, are shown in Figure 4-14. While this plate was vibrating, the field was sampled using the six microphone probe. Figure 4-15 shows the magnitude of the pressure on both measurement

planes, the first located at $z_1 = 13$ cm, and the second at $z_3 = 18$ cm. Notice that from these measurements, it is the modal structure of the plate is not at all apparent.
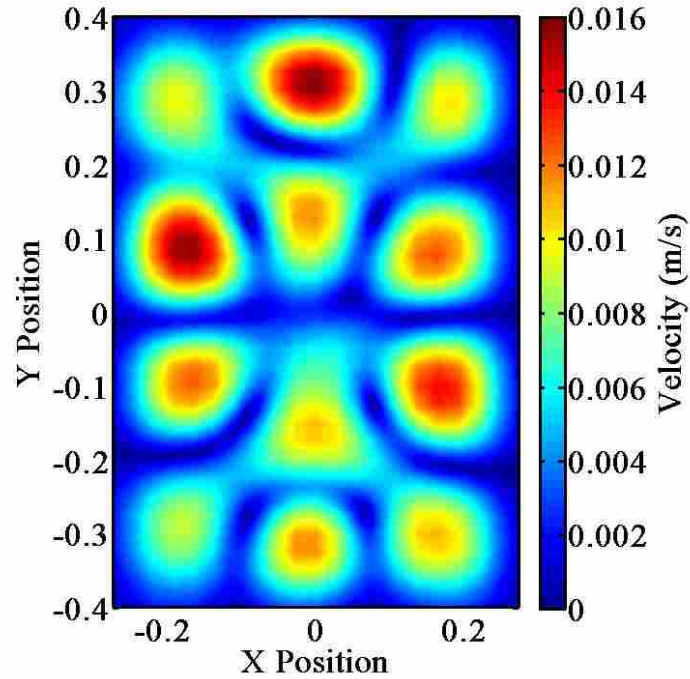
Figure 4-14: The normal velocity response of the plate measured by SLDV.
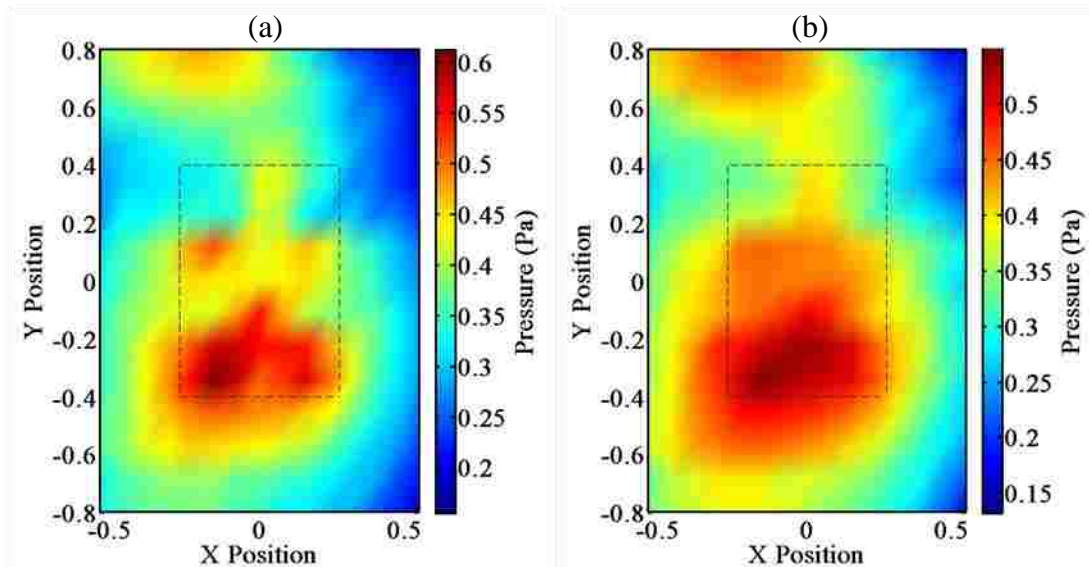
Figure 4-15: Measured pressure at (a) the $z_1 = 13$ cm plane, and (b) the $z_3 = 18$ cm plane.

By varying the number of measurement locations used to sample the field and reconstruct the normal velocity of the source, the error as a function of the number of sensors used was computed. The results from this comparison are shown in Figure 4-16. As a note, Maynard's suggested sensor spacing based on the distance from the source is 13 cm. This corresponds to 13 sensors in the x and y directions.
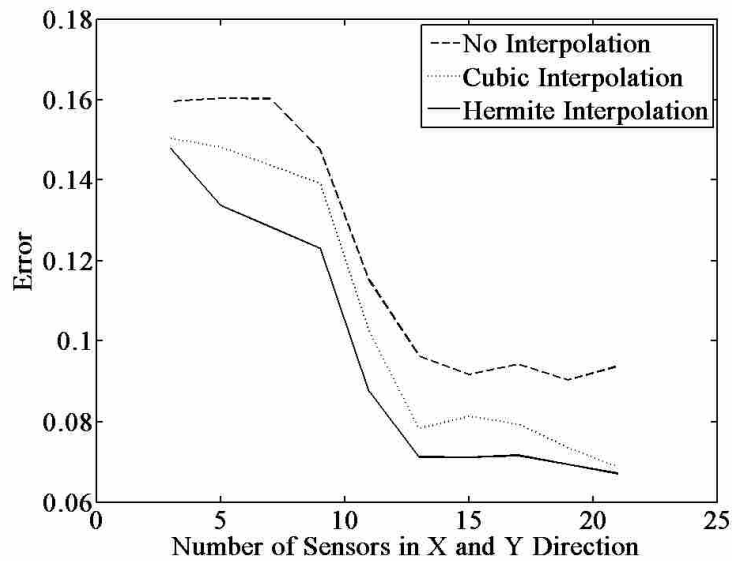
Figure 4-16: The error associated with three different interpolation schemes as a function of the number of sensors in the x and y directions.

Based on these results, the bi-cubic Hermite interpolation was able to reconstruct the particle velocity to the same degree of accuracy when 10.5 sensors are used in each direction. This corresponds to a measurement location reduction of about 35% when compared to no interpolation. The bi-cubic Hermite interpolation method also performed better than any other interpolation method for all sensor counts used. These results are consistent with the numerical simulation results.

50

4.7   Conclusions

Pressure field interpolation methods have proven to effectively increase the measurement density for an acoustic hologram. A measurement method has been proposed for interior Fourier NAH which utilizes a six microphone probe to simultaneously measure the pressure on two planes as well as estimate the pressure gradient on a third plane between the two measurement planes. Approximating the pressure gradients by using measurements on a third plane between the two measurement planes does not add a significant amount of error as long as the gradient approximation plane is close to the measurement plane. Using this information, the pressure field can be interpolated on both measurement planes. This double planar pressure measurement can be used with the spatial Fourier transform separation method to separate the incoming and outgoing waves when disturbing sources or reflections are present. Once separated, the pressure can be reconstructed anywhere up to the source.

The bi-cubic Hermite interpolation method has proven to reduce the number of required measurement locations by 20% to 80% depending on the spatial frequency. This interpolation method consistently provided the lowest amount of error when compared to using a cubic-spline interpolation without the use of pressure gradients and compared to no interpolation at all.

If the pressure gradient is not able to be measured, it has been shown that interpolating the hologram using a cubic spline interpolation method provides a comparable, and in most cases more accurate, reconstruction compared to when no interpolation is used.

Further research in this area could include the application of this measurement and interpolation method to other forms of NAH. It would also be useful to implement a combined particle-velocity sensor for these measurements and make a comparison between sensing the velocity directly and computing the finite-difference gradient approximation.

4.8 Acknowledgments

5 CONCLUSIONS

5.1 Summary

The spatial Fourier transform method of wave separation provides a useful means of performing interior NAH. By measuring complex pressure on two parallel planes, enough information is available to separate the waves coming from both sides of the measurement plane. This method is simple to incorporate into free-field Fourier NAH code and doesn't significantly add to the computational expense.

In order to correctly isolate and reconstruct the waves coming from one side of the measurement aperture, the radiated pressure must be equal to or greater than any radiated pressure entering the measurement aperture from the opposite side. In other words, the noise coming from a disturbing source must not be greater than the source of interest.

For an accurate separation, the measurement planes must be closely spaced. Simulations showed that for best results, the measurement planes should be spaced no more than 40% of the acoustic wavelength from each other.

The amount of allowable noise in a measurement is dependent on the spatial distribution of pressure. Large spatial variation requires a larger signal to noise ratio. For some cases, the noise must be at least 30 dB lower than the signal.

Pressure field interpolation methods have proved to effectively increase the measurement density for an acoustic hologram. A measurement method has been proposed for interior Fourier

NAH which utilizes a six microphone probe to simultaneously measure the pressure on two planes as well as estimate the pressure gradient on a third plane between the two measurement planes. Approximating the pressure gradients by using measurements on a third plane between the two measurement planes doesn't add a significant amount of error as long as the gradient approximation plane is close to the measurement plane. Using this information, the pressure field can be interpolated on both measurement planes. This double planar pressure measurement can be used with the spatial Fourier transform separation method to separate the incoming and outgoing waves when disturbing sources or reflections are present. Once separated, the pressure can be reconstructed next at the source.

The bi-cubic Hermite interpolation method has proved to reduce the number of required measurement locations by 20% to 80% depending on the spatial frequency. This interpolation method consistently provided the lowest amount of error when compared to using a cubic-spline interpolation without the use of pressure gradients and compared to no interpolation at all.

If the pressure gradient is not able to be measured, it has been shown that interpolating the hologram using a cubic-spline interpolation method provides a comparable, and in most cases more accurate, reconstruction compared to when no interpolation is used.

5.2 Recommendations

There are many opportunities to conduct further research in the area of interior NAH. On the subject of the spatial Fourier transform separation technique, it would be helpful to take into account the inclusion of secondary reflections, side reflections, and/or scattering off of the primary source. This would allow more accurate reconstructions to take place. It would also benefit the field to investigate the effects of measurement position error, and microphone

calibration error on the separated field. Adaptations of this separation method to other NAH techniques such as IBEM, HELS, or SONAH would be useful to expand its usefulness.

Further work in the area of energy-based sensing, such as a comparison between a pressure gradient sensor and the device Microflown for measuring the particle velocity, would be useful. Previous work using Microflown was performed previously, but these two gradient approximation techniques have not been compared. Application of this interpolation method to other forms of NAH would be useful to those using those techniques.

REFERENCES

[1] J. Y. Chung, "Cross-spectral method of measuring acoustic intensity without error caused by instrument phase mismatch," *Journal of the Acoustical Society of America*, vol. 64, no. 6, pp. 613-616, 1978.

[2] J. C. Chen, K. Yao, and R. E. Hudson, "Source localization and beamforming," *IEEE Signal Processing Magazine*, vol. 19, no. 2, pp. 30–39, 2002.

[3] P. A. Nelson, and S. H. Yoon, "Estimation of acoustic source strength by inverse methods: Part I, Conditioning of the inverse problem," *Journal of Sound and Vibration*, vol. 233, no. 4, pp. 643-668, 2000.

[4] M. R. Bai, "Application of BEM (boundary element method)-based acoustic holography to radiation analysis of sound sources with arbitrarily shaped geometries," *Journal of the Acoustical Society of America*, vol. 92, no. 1, pp. 533-549, 1992.

[5] W. A. Kuperman, W. S. Hodgkiss, H. C. Song, T. Akal, C. Ferla, D. R. Jackson, "Phase conjugation in the ocean: Experimental demonstration of an acoustic time-reversal mirror," *Journal of the Acoustical Society of America*, vol. 103, no. 1, pp. 25-40, 1998.

[6] S. F. Wu, "Methods for reconstructing acoustic quantities based on acoustic pressure measurements," *Journal of the Acoustical Society of America*, vol. 124, no. 5, pp. 2680-2697, 2008.

[7] E. G. Williams, J.D. Maynard, and E. Skudrzyk, "Sound source reconstruction using a microphone array," *Journal of the Acoustical Society of America*, 68, 340-344 (1980).

[8] W. A. Veronesi, and J. D. Maynard, "Digital holographic reconstruction of sources with arbitrarily shaped surfaces,'' *Journal of the Acoustical Society of America*, vol. 85, no. 2, pp. 588-598, 1989.

[9] G. T. Kim, and B. H. Lee, "3-D sound source reconstruction and field reprediction using the Helmholtz integral equation," *Journal of Sound and Vibration*, vol. 136, no. 2, pp. 245-261, 1990.

[10] Z. Wang and S.F. Wu, "Helmholtz equation-least squares method for reconstructing the acoustic pressure field," *Journal of the Acousical Society of America*, vol. 102, no. 4, pp. 2020-2032, 1997.

[11] Y. T. Cho, J. S. Bolton, and J. Hald, "Source visualization by using statistically optimized near-field acoustical holography in cylindrical coordinates," *Journal of the Acoustical Society of America*, vol. 118, no. 4, pp. 2355-2364, 2005.

[12] M. Villot, G. Chaveriat, and J. Roland, "Phonoscopy: An acoustical holography technique for plane structures radiating in enclosed spaces," *Journal of the Acoustical Society of America*, vol. 91, no. 1, pp. 187-195, 1992.

[13] Y. K. Kim, Y. H. Kim, "Holographic reconstruction of active sources and surface admittance in an enclosure," *Journal of the Acoustical Society of America*, vol. 105, no. 4, pp. 2377-2383, 1999.

[14] E. G. Williams, B. H. Houston, P. C. Herdic, S. T. Raveendra, and B. Gardner, "Interior near-field acoustical holography in flight," *Journal of the Acoustical Society of America*, vol. 108, no. 4, pp. 1451-1463, 2000.

[15] F. Jacobsen, V. Jaud, "Statistically optimized near field acoustic holography using an array of pressure-velocity probes," *Journal of the Acoustical Society of America*, vol. 121, no. 3, pp. 1550-1558, 2007.

[16] Y. B. Zhang, X. Z. Chen, and F. Jacobsen, "A sound field separation technique based on measurements with pressure-velocity probes," *Journal of the Acoustical Society of America*, vol. 125, no. 6, pp. 3518-3521, 2009.

[17] M. Tamura, "Spatial Fourier Transform method of measuring reflection coefficients at oblique incidence. I. Theory and numerical examples," *Journal of the Acoustical Society of America*, vol. 88, no. 5, pp. 2259-2264, 1990.

[18] M. Tamura, J. F. Allard, and D. Lafarge, "Spatial Fourier Transform method of measuring reflection coefficients at oblique incidence. II. Experimental Results," *Journal of the Acoustical Society of America*, vol. 97, no. 4, pp. 2255-2262, 1995.

[19] M. T. Cheng, J. A. Mann III, and A. Pate, "Sensitivity of the wave-number domain field separation methods for scattering," *Journal of the Acoustical Society of America*, vol. 99, no. 6, pp. 3550-3557, 1996.

[20] M. C. Harris, J. D. Blotter, and S. D. Sommerfeldt, "Obtaining the complex pressure field at the hologram surface for use in near-field acoustical holography when pressure and in-plane velocities are measured," *Journal of the Acoustical Society of America*, vol. 119, no. 2, pp. 808-816, 2006.

[21] E. G. Williams, *Fourier Acoustics, Sound Radiation and Nearfield Acoustical Holography*, Academic Press, San Diego, CA, 1999.

[22] M.-T. Cheng, J. A. Mann III, and A. Pate, "Wave-number domain separation of the incident and scattered sound field in Cartesian and cylindrical coordinates," *Journal of the Acoustical Society of America*, vol. 97, no. 4, pp. 2293-2303, 1995.

[23] D. Hallman, and J. S. Bolton, "A Technique for Performing Source Identification in a Reflective Environment by Using Nearfield Acoustical Holography," *From the Proceedings of Noise-Con,* pp. 479-484, 1993.

[24] D. L Hallman, J. S. Bolton, S. M. Dumbacher, D. L. Brown, B. W. Libbey, and M. J. Lally, "Acoustic Source Location in Vehicle Cabins and Free-field with Nearfield Acoustical Holography via Acoustic Arrays," *From the Proceedings of the 19th International Seminar on Modal Analysis,* Leuven, Belgium, vol. 2, pp. 841-851, 1994.

[25] D. Hallman, J. S. Bolton, L. B. Long, and H. Takata, "The Application of Nearfield Acoustical Holography to Locate Sources in Enclosed Spaces Exhibiting Acoustic Modal Behavior," *Proceedings of the 12th International Modal Analysis Conference*, pp. 1076-1082, 1994.

[26] S. Dumbacher, J. Blough, D. Hallman, and P. Wang, "Source Identification Using Acoustic Array Techniques," *From the Proceedings of the SAE Noise and Vibration Conference*, vol. 2, pp. 1023-1035, 1995.

[27] Y. H. Kim, "Can we hear the shape of noise," *Plenary Lecture, The 18th International Congress on Acoustics*, Kyoto International Conference Hall, Japan, 2004.

[28] F. Jacobsen, X. Chen, V. Jaud, "A comparison of statistically optimized near field acoustic holography using single layer pressure-velocity measurements and using double layer pressure measurements," *Journal of the Acoustical Society of America,* vol. 123, no. 4, pp. 1842-1845, 2008.

[29] E. G. Williams, "Regularization methods for near-field acoustical holography," *Journal of the Acoustical Society of America*, vol. 110, no. 4, pp. 1976-1988, 2001.

[30] E. G. Williams, "Continuation of acoustic near-fields," *Journal of the Acoustical Society of America*, vol. 113, no. 3, pp. 1273-1281, 2003.

[31] B. K. Gardner and R. J. Bernhard, "A noise source identification technique using an inverse Helmholtz integral equation method," *ASME J. Vib., Acoust., Stress, Reliab. Des.*, vol. 110, pp. 84–90, 1988.

[32] J. Hald, "Patch holography using a two-layer handheld array with an extended SONAH algorithm," *Proceedings of Euronoise*, Tampere, Finland, 2006.

[33] Z. A. Collins, K. L. Gee, S. D. Sommerfeldt, and J. D. Blotter, "Investigation of the spatial Fourier transform separation method for use in interior near-field acoustical holography," manuscript submitted for publication to *Journal of the Acoustical Society of America.* Oct. 2010.

[34] J. D. Maynard, E. G. Williams, and Y. Lee, "Nearfield acoustic holography I. Theory of generalized holography and the development of NAH," *Journal of the Acoustical Society of America*, vol. 78, no. 4, pp. 1395-1413, 1985.

APPENDIX A. ASSEMBLING THE PORTABLE LINEAR POSITIONING UNIT

As experimental procedures necessitated, a portable linear positioning unit has been designed to automatically position an array of microphones and record pressure measurements at any number of predetermined positions along a two-dimensional plane. Due to a lack of hardware documentation, the following instructions are provided to aid in the assembling and disassembling of this piece of equipment. Most parts and materials are listed in Table A-1. Just because this equipment is labeled as "portable" doesn't mean setup is trivial. Plan on a few hours to get everything setup.

Table A-1: Portable Scanning System Bill of Materials

Item Description	Supplier	Manufacturer / Part Name / Number	QTY.
Linear Positioning Unit	Minarik Automation and Control	Macron Dynamics Inc. S/N: 12095 P/N: MGS14SP000012040	1
Stepper Motor Drives	Minarik Automation and Control	Applied Motion Products / Stac6 Si	2
Stepper Motors	Minarik Automation and Control	Applied Motion Products / HT23-550D	2
Inductive Sensors	Minarik Automation and Control	Turck / Ni3.5 - Q5.5 - RN6X	6
Stepper Motor Brake	Minarik Automation and Control	Inertia Dynamics LLC / 8923-3331 12 VDC	1
Support Stand Legs	Fiero Fluid Power Inc.	80/20 / Extruded 4080 / 40-4080-1.524m	3
Plastic End Caps	Fiero Fluid Power Inc.	80/20 / 4080 End Caps / 40-2045	6
Corner Bracket	Fiero Fluid Power Inc.	80/20 / In Gusset Bkt. / 40-4336	6
T-Nuts/Bolts	Fiero Fluid Power Inc.	80/20 / T-Nuts/Bolts / 75-3422	24
12V Power Supply	Peak to Peak Power	S-100F-12	1
Motor Cable Extensions	Digi-Key	General Cable / SHIELDED 24AWG UL2464 8 COND / C0744A-12-10	100'

For setup, the major parts have been labeled, they include:

- Side supports (A1, A2)
- Top and bottom supports (B1, B2)
- X axis cross bar (C1)
- Vertical Positioning Stands (D1, D2, D3)

Assembly

1. Lay out parts A1 and A2 about eight feet away from each other as shown with A1 to the
   left of A2. Put two supporting blocks of wood underneath the tops of the pieces (the
   'top' is the end with the part label on it).
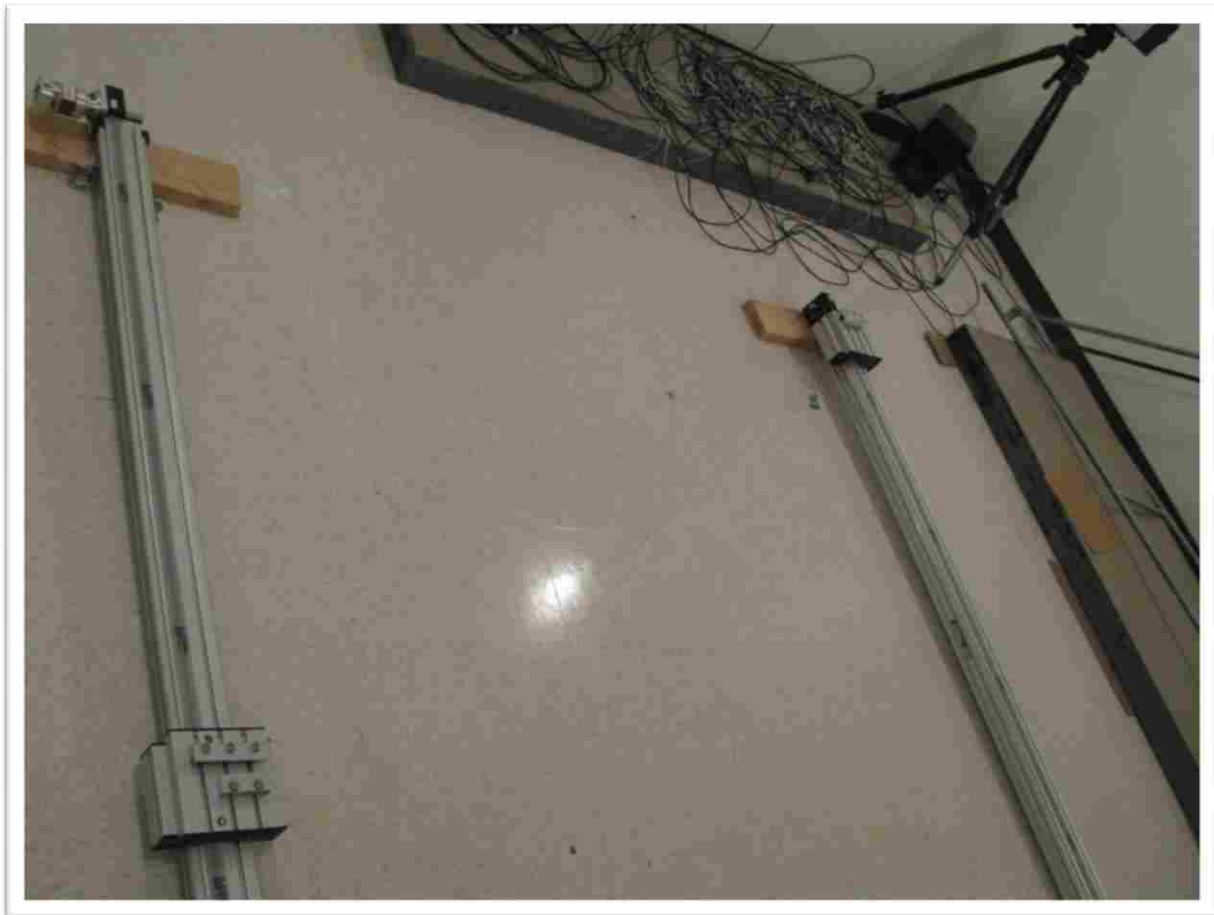
Figure A-1: Illustration of step 1.

2. Position part B2 between the 'bottom' of parts A1 and A2 with the label facing towards the ceiling. Loosen, the bolts on the bottom of A1 and A2 (Figure 2(a)), lock part B2 in place by inserting bolts into ends of B2 and tightening the bolts (Figure 2(b)). NOTE: If the scanning system will be used vertically, tighten these bolts extremely tight to avoid unwanted torque on the bolts.

(a)

(b)

Figure A-2: Illustration of step 2.

3. Position the mounting brackets (connected to the drive belts) on parts A1 and A2 to the bottom of the scanning system (Figure 3). By pushing them all of the way to the rubber stops, the mounting brackets will be aligned with each other which allows the stepper motors to drive the system easier.

(a)
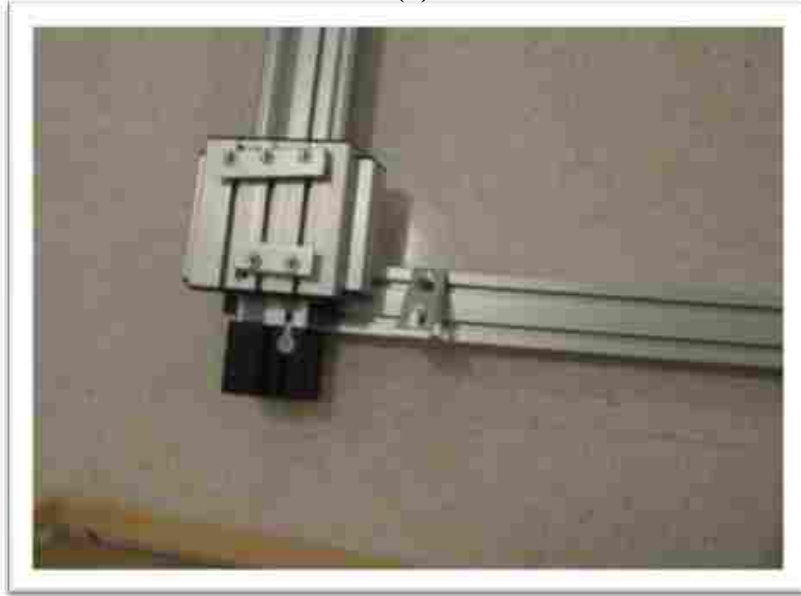
(b)
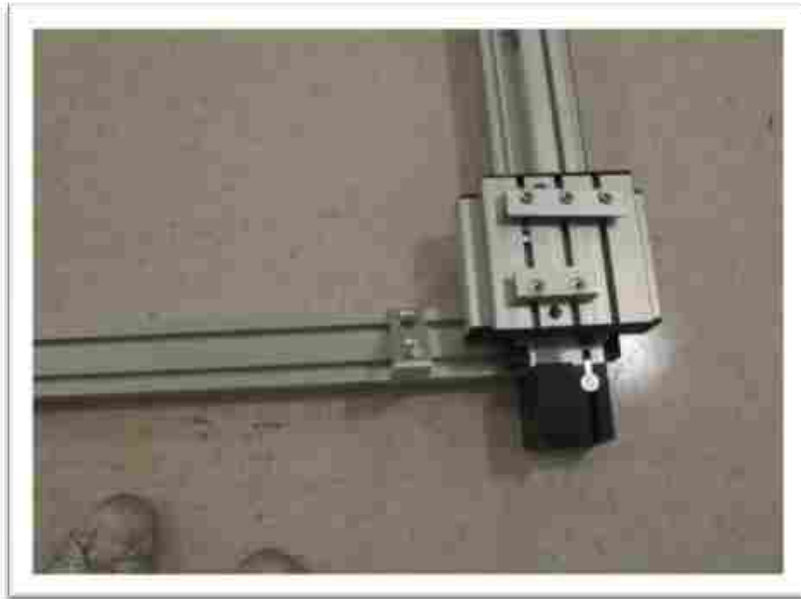
Figure A-3: Illustration of step 3.

4. Position part B1 at the 'top' of parts A1 and A2 with the label facing towards the ceiling. The bar connected to B1 should line up with the shafts of the drive belts on parts A1 and A2. Position and tighten B1 so that the shafts line up with each other (Figure 4).
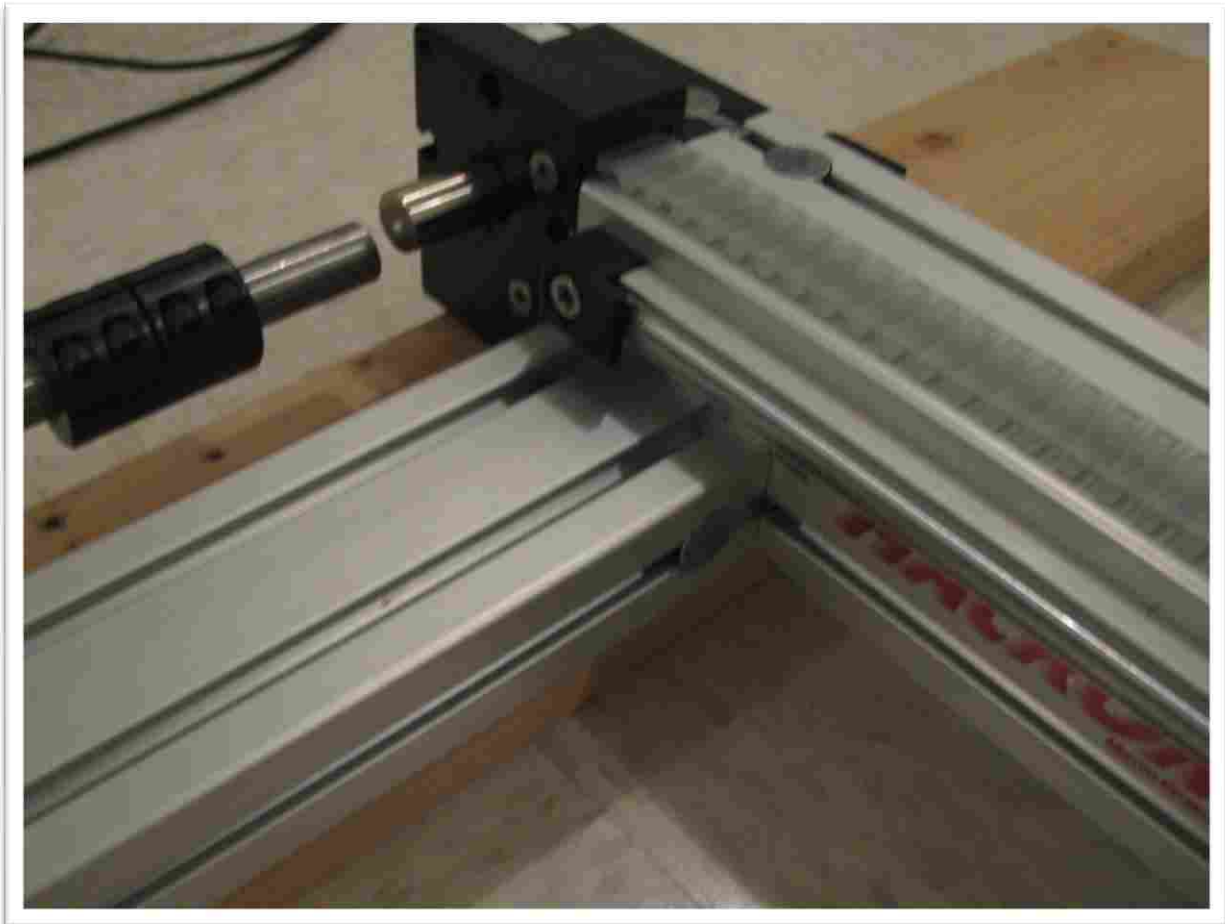
Figure A-4: Illustration of step 4.

5. Loosen the black sleeves on either end of the bar and slide over shafts so that it equally covers both shafts (Figure 5). Tighten the sleeve extremely hard to ensure the scanning system doesn't slip when used vertically.

Figure A-5: Illustration of step 5.

6. Place the X axis (part C1) on top of mounting brackets found on A1 and A2 (Figure 6). Make sure the gear box (the round aluminum piece with red wrapping) is on the left side of the scanning system. This should be the same side as the Y axis gear box.

Figure A-6: Illustration of step 6.

7. Lock the X axis into place by loosening the mounting brackets and sliding them into the slots on the rails (Figure 7). Tighten the bolts so that the X axis arm is secure.

Figure A-7: Illustration of step 7.

8. If the scanning system will be used lying horizontally, move on to step 12. If the scanning system will need to be raised vertically, then proceed to step 9.

9. With the help of others, lift the 'top' end of the scanning system up until it is standing vertically supported by the black caps of parts A1 and A2.

10. Slide parts D1, D2, and D3 underneath the scanning system and align their brackets with the brackets already attached to part B2. Screw bolts through brackets into nuts inside of the rails (Figure 8). NOTE: Also tighten these bolts extremely well to increase stability.

Figure A-8: Illustration of step 10.

11. Raise X axis up about 2 feet and support with 2x4's (Figure 9). This will allow clearance to attach the stepper motor to the X axis.

Figure A-9: Illustration of step 11.

12. Slide the Y axis stepper motor and brake into the Y axis gear box. Tighten the shaft in the gear box by inserting an allen wrench into hole in side of gear box (Figure 10). Make sure this is extremely tight to ensure the shafts don't slip, otherwise, the X axis cross-bar might fall to the ground. NOTE: you might need to raise the X axis cross-bar slightly so the shaft rotates until the set screw is visable.

Figure A-10: Illustration of step 12.

13. Secure the brake/stepper motor by inserting and tightening 4 screws. After motor is secure, attach the limit switch cable (the 9 pin serial connector) to the Y axis limit switches (Figure 11).
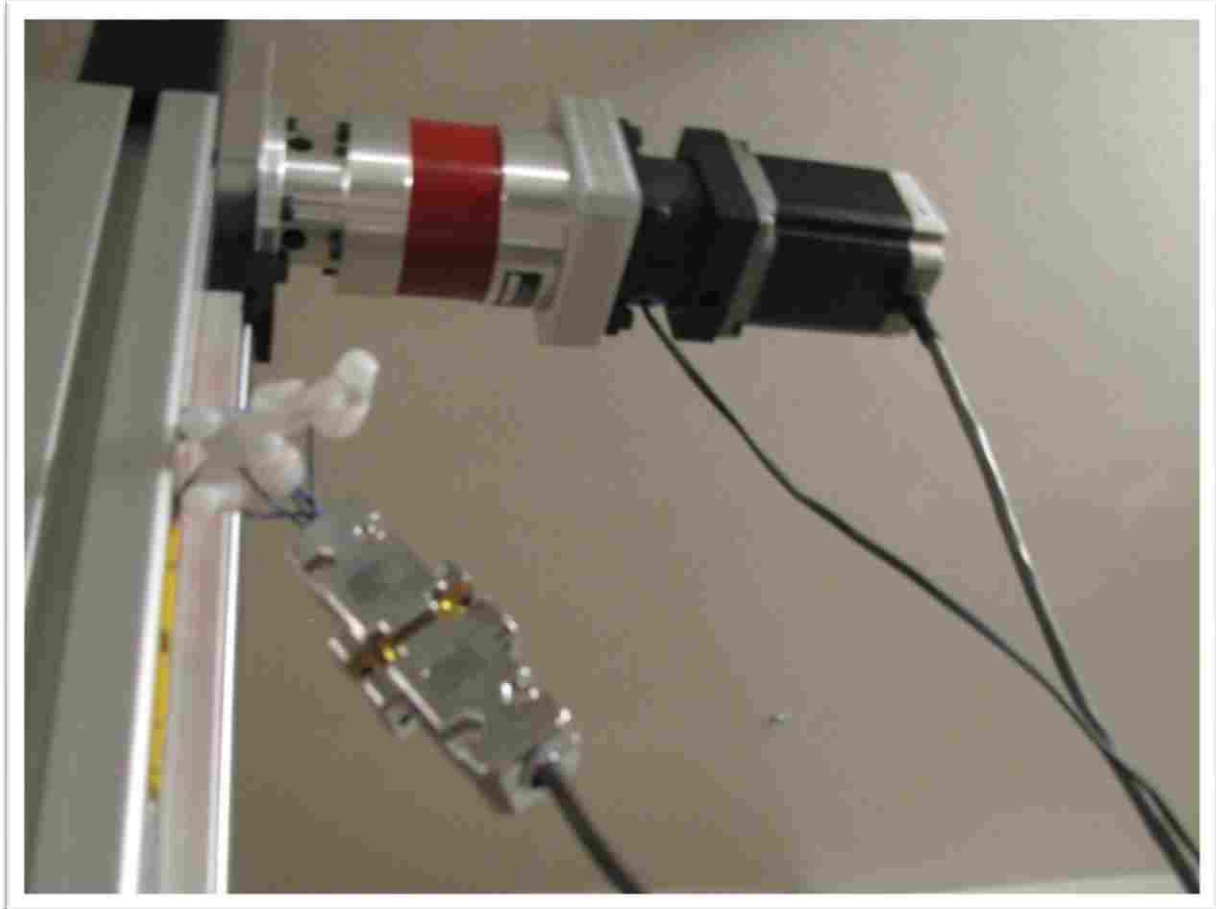
Figure A-11: Illustration of step 13.

14. Repeat steps 12 and 13 for the X axis motor.

15. Make sure all wires going to the X axis will not snag when the Y axis is in motion. Ensure there is enough slack in the wires for the Y axis to move to the home position.

16. Attach any microphone array or other device to the X axis mounting plate. Make sure any wires going to the device have enough slack for a full range of movement (Figure 12). NOTE: It may be necessary to anchor the wires to the mounting board so the device is not pulled out of place by the wires.
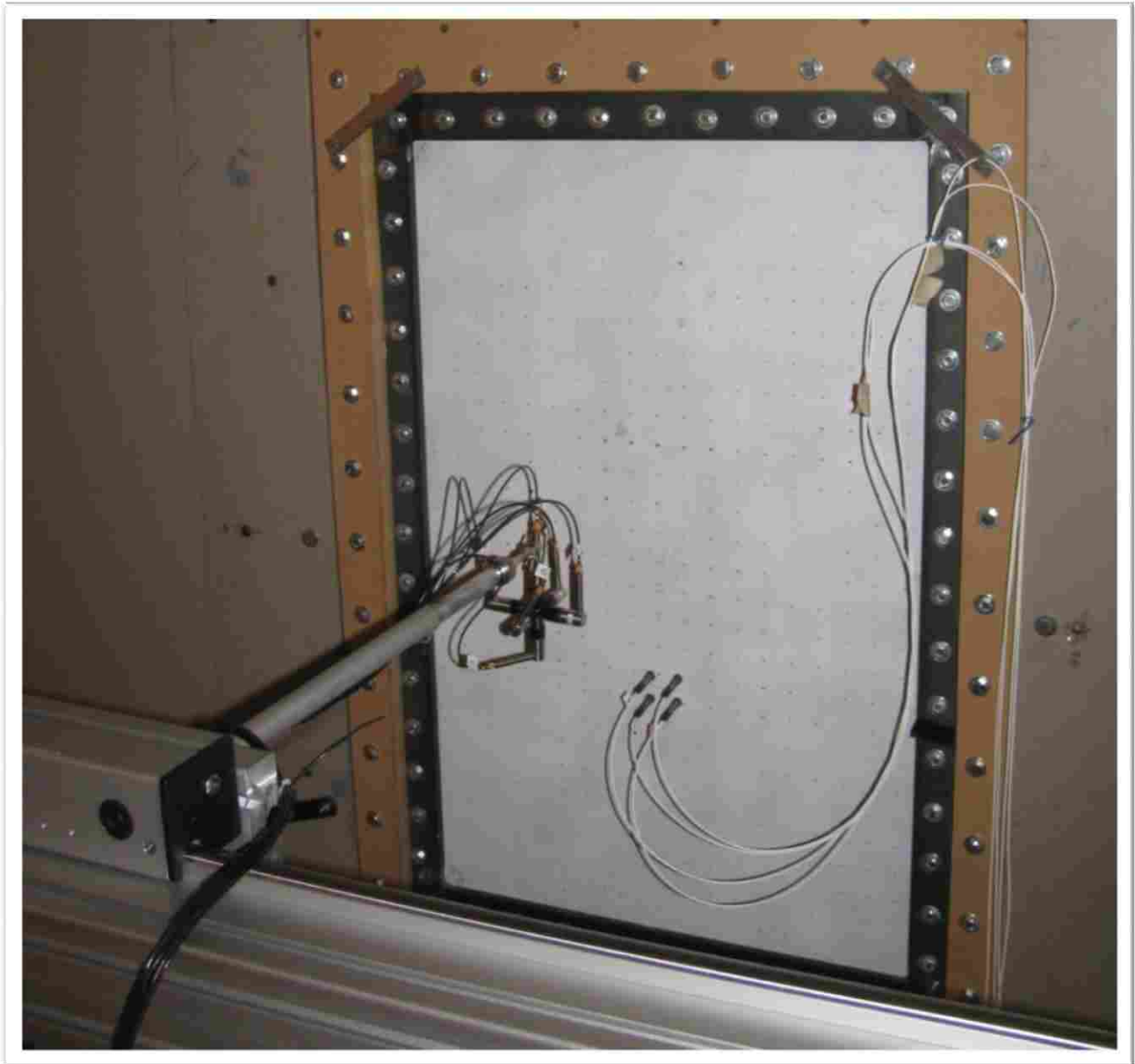
Figure A-12: Illustration of step 16.

17. Connect cord from "PC/MMI" slot in each STAC6 to serial port on computer. If only one serial port is available, use the Serial-USB adaptor included. Note: Use of the Serial-USB adaptor requires the installation of a driver.

18. Plug in power cords to both STAC6's

19. Turn on computer. Go to Control Panel > System > "Hardware" tab > Device Manager. Expand the "Ports" list. It should list which serial ports are in use. Make sure you write down which port the X axis is plugged into and which port the Y axis is plugged into. You can check which is which by disconnecting the serial connection from the computer and it will disappear from the "Ports" list.

20. Make sure you are able to send the correct commands to the correct port. Open the file, "FUNCTION Send Command to X Motor". Open the block diagram.
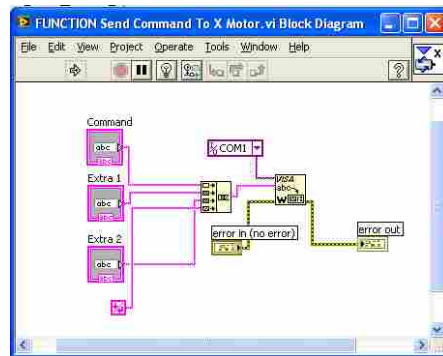
Figure A-13: The "FUNCTION Send Command To X Motor.vi" Block Diagram

Change the VISA Resource Name to the communication port the X axis is plugged into. Repeat this step, changing the VISA Resource Name to the appropriate communication port for each of the following files:

- "FUNCTION Send Command to Y Motor",

- "FUNCTION Receive Info from X Motor", and

- "FUNCTION Receive Info from Y Motor."

73

21. Plug in power cord for 12 VDC power supply.

22. Make sure all inductor sensors are operating correctly, check all six sensors to make sure they are lit up. Warning: the malfunction of any of these sensors could cause serious damage to the scanning system.

23. Make sure any microphones are connected through their respective chassis to the computer.

24. You have now completed all necessary steps for assembling the scanning system. Continue on to Appendix B for instructions on how to use the software.

APPENDIX B. USING SCANNING SYSTEM SOFTWARE

1. Once the scanning system is setup using Appendix A, the following instructions will be helpful in using the portable scanning system.

2. Open the latest version of the software. Currently, the latest version is "!PortableScanningSystemv1.1.vi"

3. Click the 'run' button. Go to the "Channel Setup" tab.
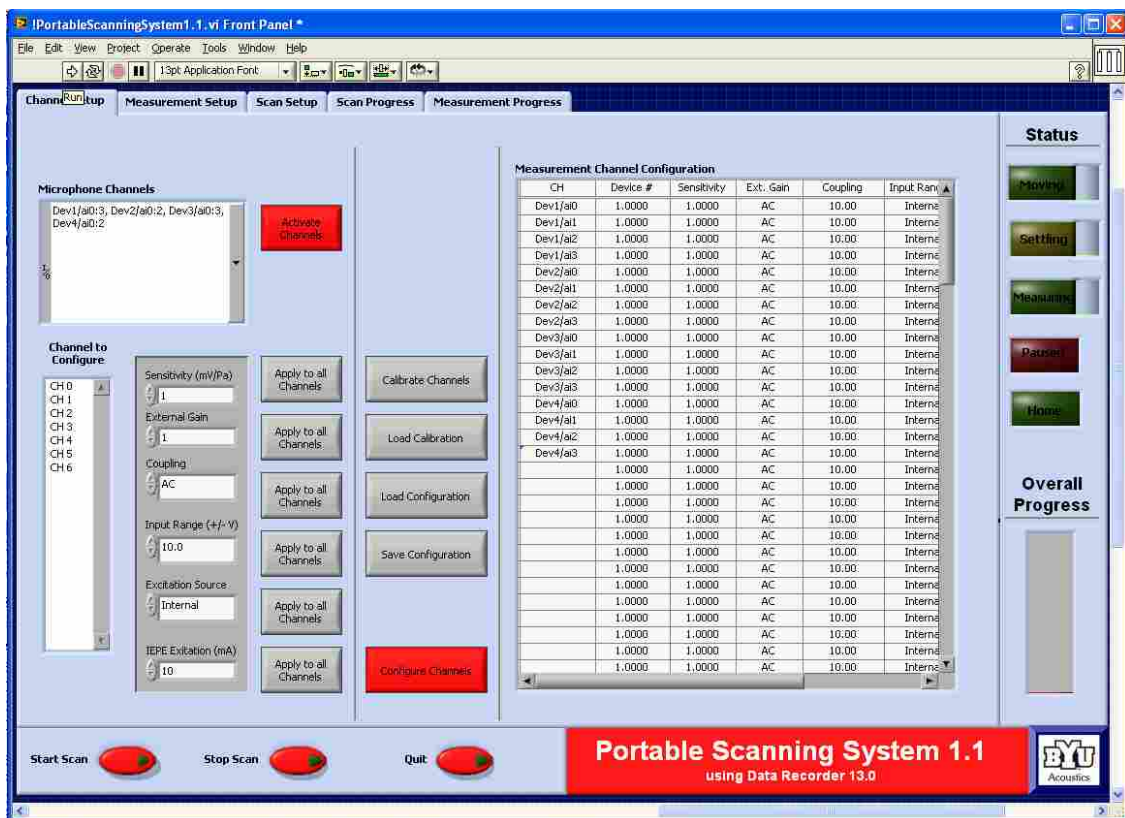
Figure B-1: The Channel Setup tab.

4. Click on the down arrow on the right side of the "Microphone Channels" box. Select all desired input channels from an NI chassis. Note: to select more than one channel, click "Browse" then hold down "Ctrl" key while selecting desired channels.

5. Click "Activate Channels." This will load the desired channels into the "Measurement Channel Configuration" box to the right.

6. Configure each channel by highlighting the desired channel in the "Channel to Configure" box, then enter desired information in configuration boxes. Press "Enter" after each entry, or click "Apply to all Channels," to use the entered value for every channel.

7. If you plan on using the same channel configuration later, it is suggested to save your configuration. Click "Save Configuration" and enter the desired filename, make sure the filename includes the extension ".txt"

8. To calibrate the microphones, click on "Calibrate Channels" and follow the instructions.

9. **Click "Configure Channels."** If this button is not clicked, the channels are not configured and the scan will not work.

10. Move on to the "Measurement Setup" tab.
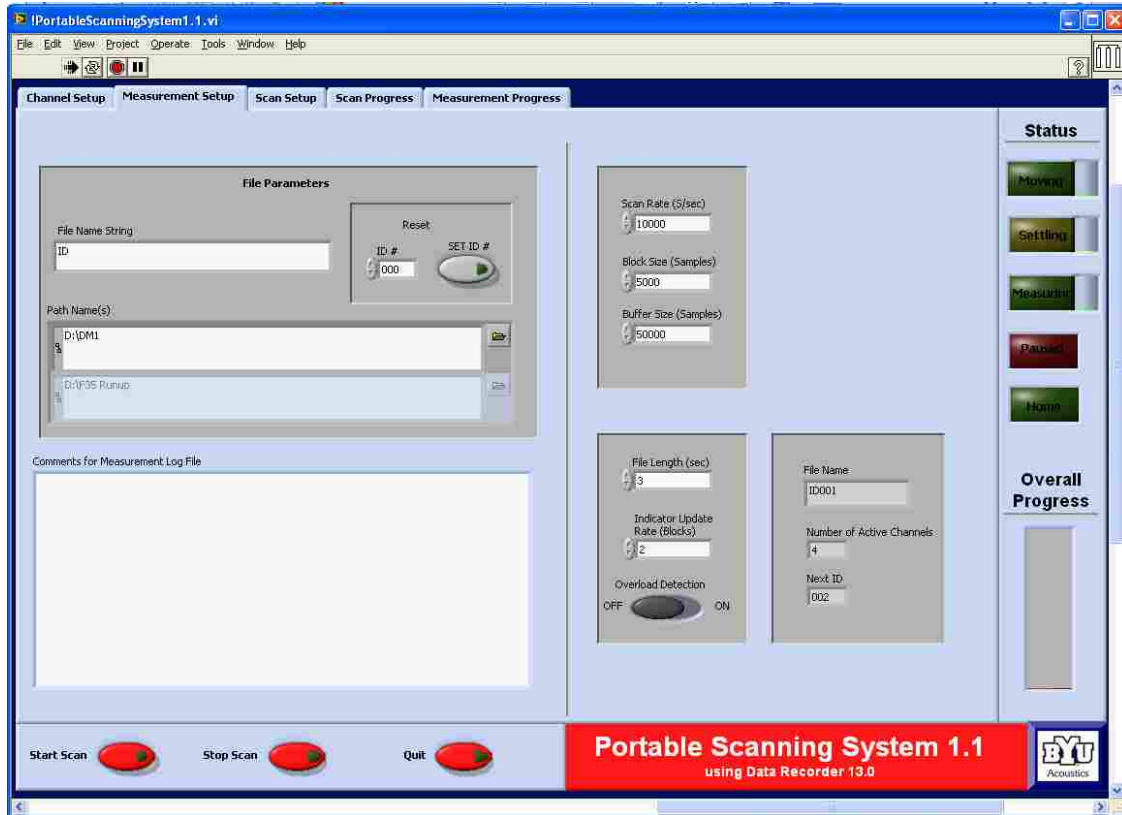
Figure B-2: The Measurement Setup tab.

11. Click the folder icon under "Path Name(s)." Select the desired home directory to save all data files.

12. If desired, enter a root name for the files in the "File Name String" box. Files will be saved according to the following syntax "Rootname00X_00Y.bin" where 00X is the measurement number and 00Y is the channel number. For example, if the root name is "Test_", and it is starting a new scan, the data for channel 3 is located at: "Test_001_003.bin"

13. Enter the desired scan rate, block size, buffer size, and file length in the appropriate boxes. Make sure the type of DAQ chassis you are using supports "Overload Detection." If it doesn't, make sure to turn this switch off.

14. Continue on to the "Scan Setup" tab.
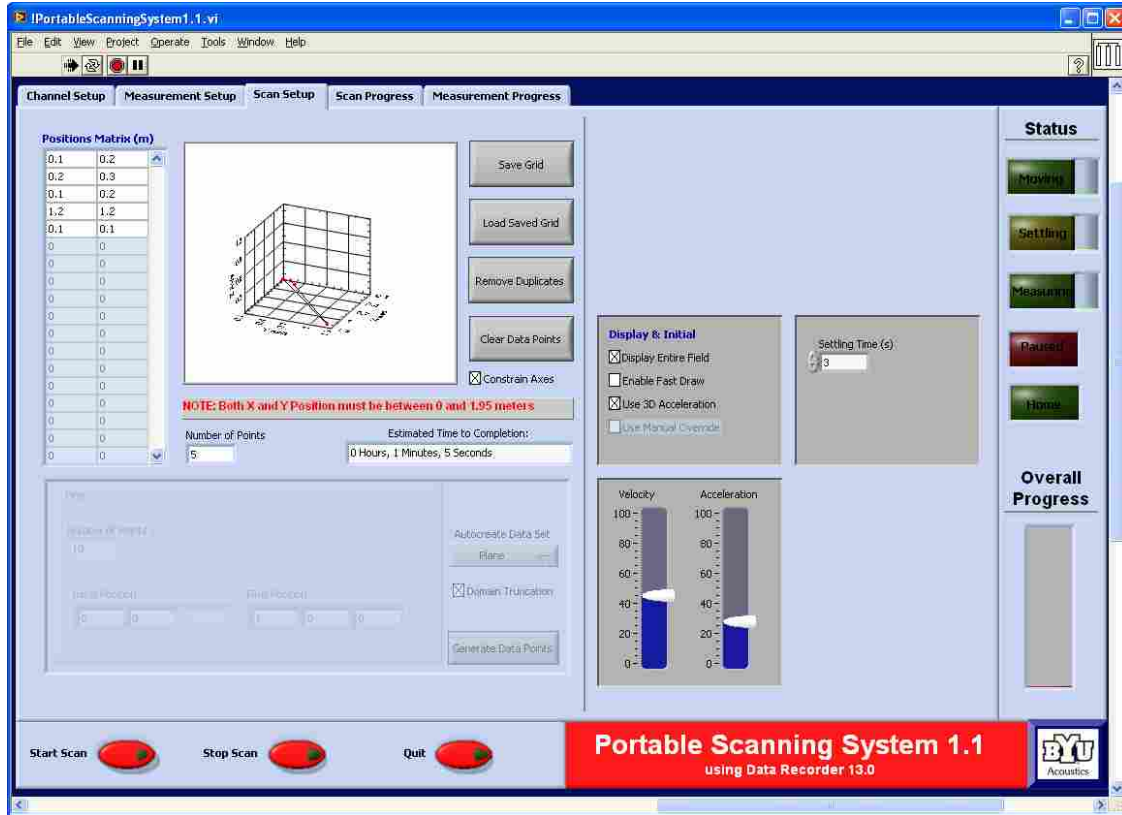
Figure B-3: The Scan Setup tab.

15. Enter scan positions by hand into the "Positions Matrix" or load a saved measurement grid. If a grid is entered in by hand, it can be saved for future use by clicking on "Save Grid." Note: Only measurement points between 0 and 1.7 m will be accepted.

16. Adjust the "Velocity" and "Acceleration" to desired values. Note: The "Estimated Time to Completion" is shown and updated based on the distance between positions, the measurement length, the settling time, and the velocity.

17. When ready to begin, click "Start Scan" button. A dialogue box will appear asking your permission to begin. The scanning system will begin moving as soon as the "Begin" button is pressed. WARNING: make sure there is nothing that would inhibit the scanning system from moving across its entire range!

18. Watch the scanning system to make sure it stops at the Home position before continuing to the specified points.

19. Watch the progress of the measurement using the "Scan Progress" tab and "Measurement Progress" tab. Note: Only time waveform data is stored in binary form. The pressure magnitudes from each channel and the FFT data are just for visual purposes during the measurement. That information can be post-processed afterward.

20. When the system has taken measurements at each of the points, a dialog box will appear stating that it is finished.

21. Turn off all related equipment.

APPENDIX C. NUMERICAL SOURCE CODE

C.1 Interior Fourier NAH on a Simply-Supported Plate

```matlab
%%%%%%%%%%%%%%%%%%%%%%%%%%%%%%%%%%%%%%%%%%%%%%%%%%%%%%%%%%%%%%%%%%%%%%%%
% Name:    InteriorNAH_SimplySupportedPlate.m                        %
% Date:    28 June 2010                                             %
% Author: Zach Collins                                              %
%                                                                  %
% Description: This program performs Fourier NAH on the field radiated %
% from a simply supported rectangular plate.  The pressure field    %
% includes a single primary reflection off a perfectly reflecting wall.%
% The field is interpolated using the bi-cubic Hermite interpolation  %
% method and is separated by using the spatial Fourier transform wave %
% separation method.  The reconstructed pressure is compared to the   %
% actual pressure on a plane closer to the plate.                   %
%                                                                  %
% Included Functions:                                              %
% SSPlate.m              (Calculates the velocity at discrete points  %
%                         for a simply supported plate)             %
% BenchmarkPress.m       (Calculates the benchmark pressure near source)%
% CalcPress.m            (Calculates the pressure for each microphone in%
%                         a six microphone probe)                   %
%%%%%%%%%%%%%%%%%%%%%%%%%%%%%%%%%%%%%%%%%%%%%%%%%%%%%%%%%%%%%%%%%%%%%%%%

clear all;
close all;
clc;

% Variables
f =  921;              %excitation frequency [Hz]
omega = 2*pi*f;        %excitation frequency [rad/sec]
c = 343;               %speed of sound [m/s]
k = omega/c;           %acoustic wavenumber [m^-1]
rho = 1.21;            %density of air [kg/m^3]
L_x = 0.3048;          %x plate dimension [m]
L_y = 0.4572;          %y plate dimension [m]
h = 0.003175;          %plate thickness [m]
z1 = 0.02;             %distance from source to mPlane 1 [m]
z2 = 0.05;             %distance from source to first mic in ED probe [m]
zmid = z2 + .005;      %distance from source to mid plane in ED probe [m]
z3 = z2 + .01;         %distance from source to last mic in ED probe [m]
zwall = .08;           %distance from source to reflective wall [m]
deltax = .01;          %microphone spacing for x gradient
deltay = .01;          %microphone spacing for y gradient
gsize = 32;            %number of points to interpolate to
```

```matlab
psize = 2*gsize;          %number of points to zero-pad to
winwid2 = .05;            %2-D spatial window strength, set to zero to turn
off.
klim = 500;               %limit for wavenumber space plot.
alpha = .05;              %wavenumber filter roll-off control
Meas_plots = 1;           %Plot the Measurements? 1=yes, 0=no
reg_on = 1;               %regularization: 1 to activate, 0 to disable

% Calculate Source Spacing
nx = 21;                  %Number of point sources for plate in x direction
ny = 21;                  %Number of point sources for plate in y direction
dx = L_x/nx;              %Distance between point sources in x direction
dy = L_y/ny;              %Distance between point sources in y direction
x = -L_x/2:dx:L_x/2;      %location of x point sources for plate
y = -L_y/2:dy:L_y/2;      %location of y point sources for plate
S = dx * dy;              %surface point area

% Calculate Measurement Spacing
xsensors = 21;            %Number of sensors to sample field in x direction
ysensors = 21;            %Number of sensors to sample field in y direction
x1 = -L_x:(2*L_x)/(xsensors - 1):L_x;  %x measurement array locations
y1 = -L_y:(2*L_y)/(ysensors - 1):L_y;  %y measurement array locations
xdens = x1(2)-x1(1);      % horizontal microphone spacing (m)
ydens = y1(2)-y1(1);      % vertical microphone spacing (m)

% Final Comparison Spacing
x3 = linspace(-L_x/2,L_x/2,gsize/2);
y3 = linspace(-L_y/2,L_y/2,gsize/2);

% Find Velocity at Chosen Points for a Simply Supported Plate
[wfinal omega_mn] = SSPlate(L_x,L_y,h,f,nx,ny,20,20);

% Calculate Benchmark Pressure
p1 = BenchmarkPress(z1,f,wfinal,x,y,x3,y3);

% Calculate Pressure for Six Microphone Probe
[p2 pmidx1 pmidx2 pmidy1 pmidy2 p3] =
CalcPress2(f,wfinal,x1,y1,x,y,z2,zmid,z3,zwall);

% Calculate Pressure Gradients
dPdx = (pmidx2-pmidx1)/(2*deltax);
dPdy = (pmidy2-pmidy1)/(2*deltay);

% Plot Measurement Fields
if Meas_plots==1
    PlateXLines = [L_x/2 L_x/2;...
                   L_x/2 -L_x/2;...
                  -L_x/2 -L_x/2;...
                  -L_x/2 L_x/2;];
    PlateYLines = [-L_y/2 L_y/2;...
                   L_y/2 L_y/2;...
                   L_y/2 -L_y/2;...
                  -L_y/2 -L_y/2];

    figure(1)
    subplot 241
    pcolor(x3,y3,abs(p1));
```

```matlab
shading interp;
colorbar;
axis image;
title(['P1 Mag, z = ',num2str(z1)]);
hold on;
plot(PlateXLines,PlateYLines,'k--','LineWidth',1);

subplot 242
pcolor(x1,y1,abs(p2));
shading interp;
colorbar;
axis image;
title(['P2 Mag, z = ',num2str(z2)]);
hold on;
plot(PlateXLines,PlateYLines,'k--','LineWidth',1);

subplot 243
pcolor(x1,y1,abs(pmidx1));
shading interp;
colorbar;
axis image;
title(['Pmidx1 Mag, z = ',num2str(zmid)]);
hold on;
plot(PlateXLines,PlateYLines,'k--','LineWidth',1);

subplot 244
pcolor(x1,y1,abs(pmidx2));
shading interp;
colorbar;
axis image;
title(['Pmidx2 Mag, z = ',num2str(zmid)]);
hold on;
plot(PlateXLines,PlateYLines,'k--','LineWidth',1);

subplot 245
pcolor(x1,y1,abs(pmidy1));
shading interp;
colorbar;
axis image;
title(['Pmidy1 Mag, z = ',num2str(zmid)]);
hold on;
plot(PlateXLines,PlateYLines,'k--','LineWidth',1);

subplot 246
pcolor(x1,y1,abs(pmidy2));
shading interp;
colorbar;
axis image;
title(['Pmidy2 Mag, z = ',num2str(zmid)]);
hold on;
plot(PlateXLines,PlateYLines,'k--','LineWidth',1);

subplot 247
pcolor(x1,y1,abs(p3));
shading interp;
colorbar;
axis image;
```

```matlab
    title(['P3 Mag, z = ',num2str(z3)]);
    hold on;
    plot(PlateXLines,PlateYLines,'k--','LineWidth',1);
end

% check for error conditions
lambda = c/f;
if(lambda<2*max(xdens,ydens))
    disp('warning: array density not sufficient to prevent spatial
aliasing');
end

% set up input geometry
width = (xsensors-1)*xdens;
height = (ysensors-1)*ydens;

zpadx = psize/gsize;
zpady = zpadx;
gsizex = gsize;
gsizey = gsize;

x2 = linspace(-width/2,width/2,gsizex);  % interpolated location vector
y2 = linspace(-height/2,height/2,gsizey);

% Hermite Surface Fit
[row column] = size(p2);
numxsegments = row - 1;
numysegments = column - 1;

% Hermite Basis Matrix
M = [2 -2 1 1;...
    -3 3 -2 -1;...
    0 0 1 0;...
    1 0 0 0];

% Slope scaling factors
scale_t = abs(x1(1) - x1(2));
scale_s = abs(y1(1) - y1(2));
P2hreal = zeros(length(x2),length(y2));
P2himag = zeros(length(x2),length(y2));
P3hreal = zeros(length(x2),length(y2));
P3himag = zeros(length(x2),length(y2));
SS = zeros(1,512);
T = zeros(1,512);

for ii=1:numxsegments
    for jj=1:numysegments
        Q2real = [real(p2(ii,jj)) real(p2(ii+1,jj)) real(dPdx(ii,jj))*scale_t
real(dPdx(ii+1,jj))*scale_t;...
            real(p2(ii,jj+1)) real(p2(ii+1,jj+1)) real(dPdx(ii,jj+1))*scale_t
real(dPdx(ii+1,jj+1))*scale_t;...
            real(dPdy(ii,jj))*scale_s real(dPdy(ii+1,jj))*scale_s 0 0;...
            real(dPdy(ii,jj+1))*scale_s real(dPdy(ii+1,jj+1))*scale_s 0 0];

        Q2imag = [imag(p2(ii,jj)) imag(p2(ii+1,jj)) imag(dPdx(ii,jj))*scale_t
imag(dPdx(ii+1,jj))*scale_t;...
```

```matlab
            imag(p2(ii,jj+1)) imag(p2(ii+1,jj+1)) imag(dPdx(ii,jj+1))*scale_t
imag(dPdx(ii+1,jj+1))*scale_t;...
            imag(dPdy(ii,jj))*scale_s imag(dPdy(ii+1,jj))*scale_s 0 0;...
            imag(dPdy(ii,jj+1))*scale_s imag(dPdy(ii+1,jj+1))*scale_s 0 0];

        Q3real = [real(p3(ii,jj)) real(p3(ii+1,jj)) real(dPdx(ii,jj))*scale_t
real(dPdx(ii+1,jj))*scale_t;...
            real(p3(ii,jj+1)) real(p3(ii+1,jj+1)) real(dPdx(ii,jj+1))*scale_t
real(dPdx(ii+1,jj+1))*scale_t;...
            real(dPdy(ii,jj))*scale_s real(dPdy(ii+1,jj))*scale_s 0 0;...
            real(dPdy(ii,jj+1))*scale_s real(dPdy(ii+1,jj+1))*scale_s 0 0];

        Q3imag = [imag(p3(ii,jj)) imag(p3(ii+1,jj)) imag(dPdx(ii,jj))*scale_t
imag(dPdx(ii+1,jj))*scale_t;...
            imag(p3(ii,jj+1)) imag(p3(ii+1,jj+1)) imag(dPdx(ii,jj+1))*scale_t
imag(dPdx(ii+1,jj+1))*scale_t;...
            imag(dPdy(ii,jj))*scale_s imag(dPdy(ii+1,jj))*scale_s 0 0;...
            imag(dPdy(ii,jj+1))*scale_s imag(dPdy(ii+1,jj+1))*scale_s 0 0];

        mm = 1;
        while y2(mm) < y1(jj)
            mm = mm + 1;
        end
        while mm <= length(y2) && y2(mm) >= y1(jj) && y2(mm) < y1(jj+1)
            SS(mm) = (y2(mm) - y1(jj))/(y1(jj+1) - y1(jj));

            kk = 1;
            while x2(kk) < x1(ii)
                kk = kk + 1;
            end

            while kk <= length(x2) && x2(kk) >= x1(ii) && x2(kk) < x1(ii+1)
                T(kk) = (x2(kk) - x1(ii))/(x1(ii+1) - x1(ii));
                P2hreal(kk,mm) = [SS(mm)^3 SS(mm)^2 SS(mm)
1]*M*Q2real*M'*[T(kk)^3;T(kk)^2;T(kk);1];
                P2himag(kk,mm) = [SS(mm)^3 SS(mm)^2 SS(mm)
1]*M*Q2imag*M'*[T(kk)^3;T(kk)^2;T(kk);1];
                P3hreal(kk,mm) = [SS(mm)^3 SS(mm)^2 SS(mm)
1]*M*Q3real*M'*[T(kk)^3;T(kk)^2;T(kk);1];
                P3himag(kk,mm) = [SS(mm)^3 SS(mm)^2 SS(mm)
1]*M*Q3imag*M'*[T(kk)^3;T(kk)^2;T(kk);1];
                kk = kk + 1;
            end
            mm = mm + 1;
        end
    end
end

P3h = P2hreal+1i*P2himag;
P3ha = P3hreal+1i*P3himag;

% Initialize Zero-Padded Matrices
P4h = zeros(psize,psize);
P4ha = zeros(psize,psize);

% Plot Interpolated Pressure
if Meas_plots==1
```

```
figure(13)
subplot 221
pcolor(x1*100,y1*100,real(p2))
shading interp;
axis image;
colorbar;
title('Measured Real Pressure (p2)')

subplot 222
pcolor(x2*100,y2*100,real(P3h))
shading interp;
axis image;
colorbar;
title('Real Pressure Field After Hermite Surface Fit (P3h)')

subplot 223
pcolor(x1*100,y1*100,real(p3))
shading interp;
axis image;
colorbar;
title('p3 (real)')

subplot 224
pcolor(x2*100,y2*100,real(P3ha))
shading interp;
axis image;
colorbar;
title('P3ha (real)')

figure(14)
subplot 221
pcolor(x1*100,y1*100,imag(p2))
shading interp;
axis image;
colorbar;
title('p2 (imaginary)')

subplot 222
pcolor(x2*100,y2*100,imag(P3h))
shading interp;
axis image;
colorbar;
title('P2h (imaginary)')

subplot 223
pcolor(x1*100,y1*100,imag(p3))
shading interp;
axis image;
colorbar;
title('p3 (imaginary)')

subplot 224
pcolor(x2*100,y2*100,imag(P3ha))
shading interp;
axis image;
colorbar;
title('P3h (imaginary)')
```

```matlab
    end

% Apply Tukey window to rows
    twinx = tukeywin(gsizex,winwid2);
    for o = 1:gsizex
        P3h(:,o) = P3h(:,o)*twinx(o);
        P3ha(:,o) = P3ha(:,o)*twinx(o);
    end

% Apply Tukey window to columns
    twiny = tukeywin(gsizey,winwid2);
    for o = 1:gsizey
        P3h(o,:) = P3h(o,:)*twiny(o);
        P3ha(o,:) = P3ha(o,:)*twiny(o);
    end

% zero pad
    xstr = (psize-gsizex)/2+1;
    ystr = (psize-gsizey)/2+1;
    xnd = (psize+gsizex)/2;
    ynd = (psize+gsizey)/2;
    P4h(ystr:ynd,xstr:xnd)= P3h;
    P4ha(ystr:ynd,xstr:xnd)= P3ha;

% 2-D FFT
    P5h = ((2/psize)^2) * fft2(P4h);
    P5ha = ((2/psize)^2) * fft2(P4ha);

% DEFINE K-SPACE VARIABLES
%initialize k-space arrays
    kz = zeros(psize);
    K_w = ones(psize);

% calculate filter step parameters
    deltaky = 2*pi/(width*zpadx);
    deltakx = 2*pi/(height*zpady);

% define kx and ky
    kx = -(psize/2)*deltakx:deltakx:(psize/2-1)*deltakx;
    ky = -(psize/2)*deltaky:deltaky:(psize/2-1)*deltaky;

%define kz
    for ii = 1:psize
        kz(ii,:) = sqrt(k^2 - (kx(ii))^2 - (ky(:)).^2);
    end

%switch quadrants
    kz1_swap(1:psize/2,1:psize/2)=kz(psize/2+1:psize,psize/2+1:psize);
    kz1_swap(1:psize/2,psize/2+1:psize)=kz(psize/2+1:psize,1:psize/2);
    kz1_swap(psize/2+1:psize,1:psize/2)=kz(1:psize/2,psize/2+1:psize);
    kz1_swap(psize/2+1:psize,psize/2+1:psize)=kz(1:psize/2,1:psize/2);

% ENTER REGULAZATION ROUTINE IF NECESSARY
if (reg_on ==1)
% show pressure fft plot
    figure(98); clf
    surf(kx,ky,20*log10(abs(P5h)));%/( max(max(abs(P5))))));
```

```matlab
    title('p5,fftd'); shading interp; colorbar; view([0 0 1]);
    axis([-klim klim -klim klim]);
    xlabel('x dimension wavenumbers'); ylabel('y dimension wavenumbers');

% get user input to calculate k_c
    instruction ='Use cursor to identify x and y position of edge of noise
floor'
    kxc = input('enter x position ');
    kyc = input('enter y position ');
    k_c = sqrt(kxc^2 + kyc^2);
    close (98)

%create windowing function
    for ii = 1:psize/2
        for jj = 1:psize/2
            if (kx(ii))^2 + (ky(jj))^2 < (k_c)^2
                K_w(ii,jj) = 1 - 0.5*exp(-(1 - (sqrt(kx(ii)*kx(ii) + ...
                    ky(jj)*ky(jj))/k_c))/alpha);
            else
                K_w(ii,jj) = 0.5*exp((1-(sqrt(kx(ii)*kx(ii) + ky(jj)*...
                    ky(jj))/k_c))/alpha);
            end
        end
    end

% copy filter
    K_w(psize,:) = K_w(1,:);
    for ii = 1:psize/2
        for jj = 1:psize/2
            K_w(psize - ii,jj) = K_w(ii + 1,jj);
        end
    end

% copy filter
    K_w(:,psize) = K_w(:,1);
    for ii = 1:psize
        for jj = 1:psize/2
            K_w(ii,psize - jj) = K_w(ii,jj + 1);
        end
    end

end
% DONE WITH REGULARIZATION SETUP

% initialize P6 and V1
    P6fromPh = zeros(psize,psize);
    V1fromPh = zeros(psize,psize);
    P6fromPh_nr = zeros(psize,psize);
    V1fromPh_nr = zeros(psize,psize);
    P_i = zeros(psize);
    P_r = zeros(psize);
    G1 = zeros(psize,psize);
    G2 = zeros(psize,psize);

% separate incident and reflected waves
    for ii = 1:psize
        for jj = 1:psize
```

```matlab
            P_i(ii,jj) = (P5h(ii,jj) - P5ha(ii,jj)*exp(1i*(z3-
zmid)*kz1_swap(ii,jj)))*exp(-1i*(z2-zmid)*kz1_swap(ii,jj)))/(exp(1i*(z2-
zmid)*kz1_swap(ii,jj))-exp(2i*(z3-zmid)*kz1_swap(ii,jj))*exp(-1i*(z2-
zmid)*kz1_swap(ii,jj)));
            P_r(ii,jj) = P5ha(ii,jj)*exp(1i*(z3-zmid)*kz1_swap(ii,jj)) -
P_ih(ii,jj)*exp(2i*(z3-zmid)*kz1_swap(ii,jj));
        end
    end
% define propagator functions
    for ii = 1:psize
        G1(ii,:) = exp(-1i.*(kz1_swap(ii,:).*(zmid-z1)));
        G2(ii,:) = exp(-1i.*(kz1_swap(ii,:).*(z3-z1)));
    end


% apply propagator function
    for ii = 1:psize
        P6fromPh(ii,:) = P_ih(ii,:).*G1(ii,:);
        V1fromPh(ii,:) = P_ih(ii,:).*Gpv(ii,:);
        P6fromPh_nr(ii,:) = P5ha(ii,:).*G2(ii,:);
        V1fromPh_nr(ii,:) = P5ha(ii,:).*Gpv(ii,:);
    end


% Apply regularization
    P6fromPh = P6fromPh.*K_w;
    P6fromPh_nr = P6fromPh_nr.*K_w;

% Take 2-D inverse FFT on regularized propagated pressure and velocity
    P7fromPh =((psize*psize)/4)*ifft2(P6fromPh);
    P7fromPh_nr =((psize*psize)/4)*ifft2(P6fromPh_nr);

% Extract Size of Original Vibrating Plate
    P8fromPh = P7fromPh(385:640,385:640);
    P8fromPh_nr = P7fromPh_nr(385:640,385:640);

% Compute Error in NAH Reconstructions
    PError_h = p1-P8fromPh;
    PError_h_nr = p1-P8fromPh_nr;
% Compute normalized standard deviation of error;
    PError_h_std = std(std(p1 - P8fromPh))/(max(max(abs(p1))))
    PError_h_std_nr = std(std(p1 - P8fromPh_nr))/(max(max(abs(p1))));

% Plot reconstructed field
if Meas_plots==1
    figure(2)
    subplot 231
    pcolor(x3,y3,abs(p1))
    shading interp;
    axis image;
    colorbar;
    title('Measurement, p1')

    subplot 232
    pcolor(x3,y3,abs(P8fromPh))
    shading interp;
    axis image;
    colorbar;
    title('Hermite Interp, Separated')
```

89

```matlab
    subplot 233
    pcolor(x3,y3,abs(PError))
    shading interp;
    axis image;
    colorbar;
    title('Error')

    subplot 234
    pcolor(x3,y3,abs(p1))
    shading interp;
    axis image;
    colorbar;
    title('Measurement, p1')

    subplot 235
    pcolor(x3,y3,abs(P8fromPh_nr))
    shading interp;
    axis image;
    colorbar;
    title('Hermite Interp, Not Seperated')

    subplot 236
    pcolor(x3,y3,abs(PError_h_nr))
    shading interp;
    axis image;
    colorbar;
    title('Error')
end
```